J. Fluid Mech. (2022), *vol*. 949, A15, doi:10.1017/jfm.2022.763

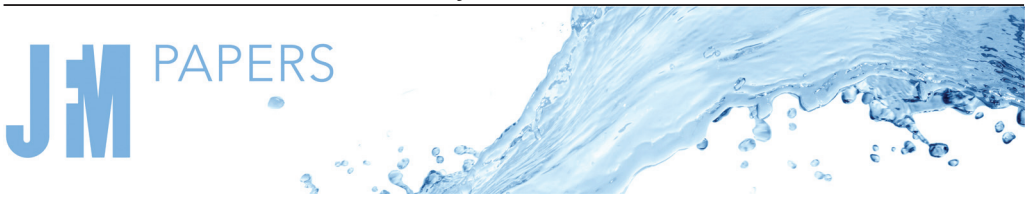

Width effect on contact angle hysteresis in a patterned heterogeneous microchannel

Xiangting Chang[1], **Haibo Huang**[1],†, **Xi-Yun Lu**[1] **and Jian Hou**[2]

[1]Department of Modern Mechanics, University of Science and Technology of China, Hefei 230026, PR China

[2]School of Petroleum Engineering, China University of Petroleum (East China), Qingdao 266580, PR China

(Received 25 October 2021; revised 16 August 2022; accepted 31 August 2022)

The width effect on contact angle hysteresis in a microchannel with patterned heterogeneous surfaces is systematically investigated. In the model, identical defects periodically appear on the background surface. To this end, a droplet's evaporation and condensation processes inside the microchannel are studied by theoretical analysis and numerical simulation based on a diffuse-interface lattice Boltzmann method. The microchannel width effect on the system's equilibrium properties is studied. The results demonstrate that the number of equilibrium configurations increases linearly with the microchannel width (b), and has a quadratic relationship with the cosine of the reference contact angle and the heterogeneity strength (ε). The average most stable contact angle is independent of b and is always equal to the contact angle predicted by the Cassie–Baxter equation. For contact angle hysteresis (H), when the microchannels are narrow and wide, there are individual-effect-dominated hysteresis (IDH) and collective-effect-dominated hysteresis (CDH), respectively. The IDH and CDH are hysteresis modes corresponding to the jumping behaviour of contact lines affected by individual defects and two neighbouring defects, respectively. Based on the graphical force balance approach, we establish a scaling law to quantify the connection between H, b and ε. Specifically, in the IDH mode, $H \sim b\varepsilon^2$, while in the CDH mode, H increases linearly with ε but nonlinearly with b.

Key words: contact lines, condensation/evaporation, drops

1. Introduction

Understanding and controlling the wetting process is of great importance for a wide range of applications, such as coating, inkjet printing, oil recovery and microfluidic devices (De Gennes 1985; Bonn *et al.* 2009). The key issue of wetting phenomena is the quantitative

† Email address for correspondence: huanghb@ustc.edu.cn

characterization of the three-phase contact line behaviour and contact angle. For a smooth and chemically homogeneous (ideal) solid surface, there is a single equilibrium contact angle, which can be described by the well-known Young's equation. However, real surfaces may have physical roughness and/or chemical heterogeneity, which would result in contact angle hysteresis (CAH) and associated complex contact line dynamics (Wang, Qian & Sheng 2008; Savva, Kalliadasis & Pavliotis 2010; Savva & Kalliadasis 2013; Savva, Groves & Kalliadasis 2019). An essential understanding has been formed that CAH is related to the existence of multiple equilibrium configurations of the fluid interface induced by the non-uniformity of a solid surface. The energy barriers between stable/metastable equilibrium configurations can trap the system in different states depending on the motion history of the contact line. In this way, the apparent contact angle may take an arbitrary value in the range $[\theta_R, \theta_A]$, where θ_R and θ_A are the receding and advancing contact angles, respectively.

Due to the importance of CAH in surface engineering, many works have been devoted to the understanding of the fundamental mechanisms of CAH from theoretical (Joanny & De Gennes 1984; Marmur 1994*a*,*b*; Gao & McCarthy 2006; Iwamatsu 2006; Xu & Wang 2011; Giacomello, Schimmele & Dietrich 2016; Hatipogullari *et al.* 2019), numerical (Crassous & Charlaix 1994; Brandon & Marmur 1996; Brandon *et al.* 2003; Kusumaatmaja & Yeomans 2007; David & Neumann 2010) and experimental (Di Meglio & Quéré 1990; Di Meglio 1992; Ramos *et al.* 2003; Priest, Sedev & Ralston 2007; Reyssat & Quéré 2009; Delmas, Monthioux & Ondarçuhu 2011; Priest, Sedev & Ralston 2013; Guan *et al.* 2016; Perrin *et al.* 2016; Wang *et al.* 2016; Lhermerout & Davitt 2018; Fuentes *et al.* 2019; Guan, Charlaix & Tong 2020) perspectives. For instance, Marmur and others investigated the CAH of a sessile droplet placed on a periodically heterogeneous surface (Marmur 1994*a*; Brandon & Marmur 1996; Montes Ruiz-Cabello *et al.* 2011). Kusumaatmaja & Yeomans (2007) numerically investigated the CAH on chemically patterned and superhydrophobic surfaces as the droplet volume was quasi-statically increased or decreased. Systematic experiments have been carried out for studying CAH on heterogeneous surfaces with a random array of defects from the microscale (Di Meglio 1992; Nadkarni & Garoff 1992; Priest *et al.* 2007; Reyssat & Quéré 2009; Priest *et al.* 2013; Fuentes *et al.* 2019) to the nanoscale (Ramos *et al.* 2003; Delmas *et al.* 2011; Lhermerout & Davitt 2018). Recently, a newly developed atomic-force-microscope measurement method (Delmas *et al.* 2011; Guan *et al.* 2016, 2020; Wang *et al.* 2016) was used to study the CAH on non-ideal long-fibre surfaces. A strong asymmetric speed dependence (Guan *et al.* 2016) as well as state and rate dependencies (Guan *et al.* 2020) of contact line dynamics were reported.

Although considerable progress has been made in understanding CAH, there are still several critical open questions. In experiments, the pinning–depinning behaviour of the contact line is usually accompanied by the occurrence of CAH (Priest *et al.* 2013). Pinning is often considered to be responsible for CAH (Delmas *et al.* 2011), or free energy barriers that cause CAH are used to explain the pinning–depinning mechanism (Orejon, Sefiane & Shanahan 2011; Zhang, Huang & Lu 2019). However, recent molecular dynamics simulations show that microscopic contact line pinning is a slowdown of contact line dynamics under the control of capillary force balance, and it may not be related to free energy barriers (Zhang, Müller-Plathe & Leroy 2015). Therefore, the relationship between microscopic pinning–depinning of the contact line and CAH has to be further explored.

It has been found that the typical gas–liquid interface (GLI) length L_i (GLI area for three-dimensional (3-D) cases) is an important physical parameter determining the hysteresis behaviour. The size effect of the GLI on CAH has attracted much attention

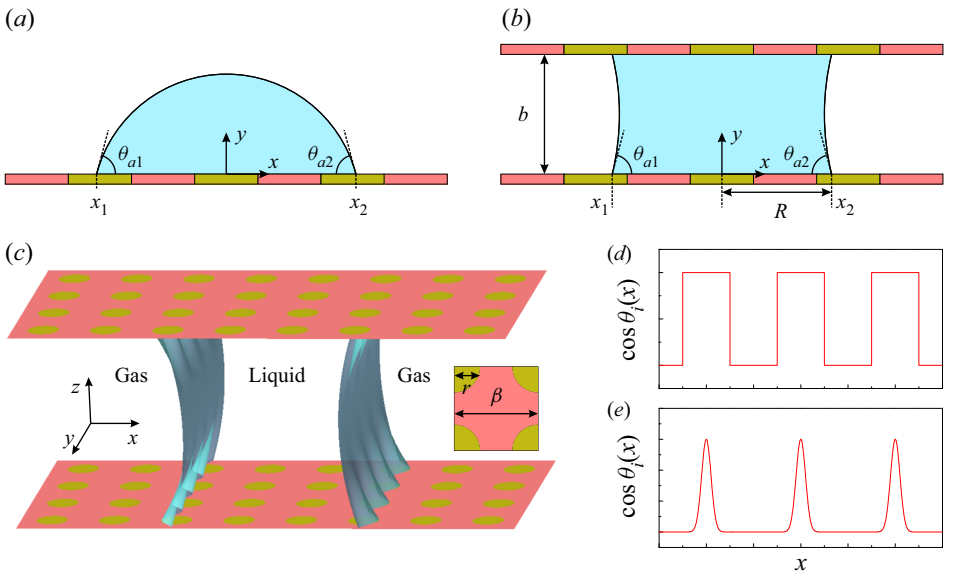

Figure 1. Schematic diagrams of (*a*) a 2-D sessile droplet placed on a chemically heterogeneous substrate, (*b*) a 2-D droplet and (*c*) a 3-D droplet confined in chemically heterogeneous microchannels. Here x_1 and x_2 represent the locations of the droplet's contact points, and the corresponding apparent contact angles are θ_{a1} and θ_{a2}, respectively. Parameter R is the base radius. The microchannel width is b and the spatial period of chemical heterogeneity is β. (*d*,*e*) Two typical 2-D surface wettability distributions.

(Quéré 2008; Ozcelik, Satiroglu & Barisik 2020). In previous studies, a sessile droplet system (see figure 1*a*) was usually chosen to study CAH by increasing or decreasing the droplet volume quasi-statically (Marmur 1994*a*; Brandon & Marmur 1996; Kusumaatmaja & Yeomans 2007; Pradas *et al.* 2016). In this circumstance, the deformation of the GLI depends not only on the properties of the solid surface but also on the droplet volume. As a result, irregular oscillatory curves would be obtained to describe the evolution of receding and advancing contact angles (Marmur 1994*a*), which is not conducive to the statistical analysis of CAH. Recently, Hatipogullari *et al.* (2019) and Xu & Wang (2011) studied CAH using a chemically heterogeneous microchannel (see figure 1*b*). The advantage of choosing this system is that the typical GLI length (approximately equal to the microchannel width) does not vary with liquid volume. Qualitatively, Xu & Wang (2011) found that on a periodically patterned microchannel, for a given microchannel width, the receding and advancing contact angles fluctuate periodically as liquid volume changes. Hatipogullari *et al.* (2019) extended the graphical force balance approach proposed by Joanny & De Gennes (1984) to two-dimensional (2-D) microchannel systems. For the size effect, they qualitatively found increasing microchannel width brings the system from a subthreshold regime, to a stick–slip-dominated regime and finally to a regime with a quasi-constant advancing and receding angle. However, there is still a lack of quantitative insight into the effect of the typical GLI length on hysteresis behaviour.

Another unresolved key problem is the complete theoretical modelling of the relationship between CAH and the properties of a substrate's disorder. For individual-effect-dominated hysteresis (IDH), i.e. contact line jumping is only affected by individual defects, Joanny & De Gennes (1984) proposed a scaling law by considering the mechanical balance of capillary force exerted by the defects (i.e. defect force) and the

elastic restoring force due to the deformation of the contact line:

$$H \propto \phi F_{d,max}^2. \tag{1.1}$$

Here ϕ is the number of defects per unit area (defect density), $F_{d,max}$ the maximum defect force and H the value of CAH. Subsequently, this scaling law was verified by experiments (Di Meglio 1992; Ramos *et al.* 2003; Delmas *et al.* 2011; Lhermerout & Davitt 2018). Hatipogullari *et al.* (2019) performed theoretical analysis on the threshold value of wettability gradients inducing hysteresis and the scaling law for the IDH mode (1.1) by using 2-D microchannels. However, if contact line jumping is affected by two neighbouring defects, it is referred to as collective-effect-dominated hysteresis (CDH). The contact line behaviour in CDH may significantly differ from that in IDH (Di Meglio & Quéré 1990; Di Meglio 1992; Reyssat & Quéré 2009). As far as we know, there is no explicit theoretical explanation for CAH under the collective effect (Quéré 2008; Bonn *et al.* 2009). This severely limits the further understanding of CAH and even wetting phenomena.

The present work is committed to exploring the open issues discussed above. To this end, we systematically investigate the quasi-static CAH in a chemically heterogeneous microchannel by theoretical analysis and numerical simulations based on a diffuse-interface method. We focus on the size effect and the related scaling laws. It is noticed that conclusions coming from chemically heterogeneous microchannels are also applicable to microchannels with physical roughness (Joanny & De Gennes 1984). Here in our study, we mainly investigate 2-D cases and then check whether the conclusions are applicable to 3-D cases.

The remainder of this paper is organized as follows. The problem statement and mathematical formulation are presented in § 2. The numerical method is described in § 3. Detailed results for 2-D and 3-D cases are discussed in §§ 4 and 5, respectively. Finally, conclusions are presented in § 6.

2. Problem statement and mathematical formulation

2.1. *Physical problem*

Here we consider the GLI motion in a microchannel with a width of b. The upper and lower walls of the microchannel are smooth, rigid and flat, but have the same periodic chemical heterogeneity (as shown in figure 1*b*,*c*). The spatial period of surface heterogeneity is β, which is the same in both horizontal directions for 3-D cases. The chemical heterogeneity is characterized by a spatially dependent intrinsic contact angle θ_i that is defined by Young's equation. Two typical 2-D surface wettability distributions are shown in figures 1(*d*) and 1(*e*), respectively. The droplet volume increases or decreases by quasi-static condensation or evaporation, which drives the GLI and contact line movements. For 2-D cases, sharp-edged defects (so-called mesa defects; see figure 1*d*) are mainly considered because they can cause a variety of contact line dynamics behaviour, and have been widely adopted in previous studies (Wang *et al.* 2008; Zhang *et al.* 2015). For 3-D microchannels, an array of circular defects is regularly distributed on the surface. In the current work, gravity is not considered.

2.2. *Mathematical formulation*

For the 2-D cases, although asymmetric phase transitions can also exist, we only consider the symmetric regimes (left–right and top–bottom). Here the GLI is approximated by a

circular arc. Then the theoretical description of the system can be performed. Because the phase transitions on the left- and right-hand sides are symmetric, the GLI and contact line motions on both sides are identical. Therefore we have $\theta_{a1} = \theta_{a2} = \theta_a$ and $x_2 = -x_1$. Here x_1 and x_2 represent the locations of the droplet's contact points, and the corresponding apparent contact angles are θ_{a1} and θ_{a2}, respectively. Defining base radius as $R = (x_2 - x_1)/2$, we have the volume of liquid (it is actually the cross-sectional area for 2-D cases) given by

$$V(R) = 2Rb + b^2 \frac{2\theta_a - \pi + \sin 2\theta_a}{4\cos^2\theta_a}. \tag{2.1}$$

In order to analyse the stability of the system, the interfacial free energy is calculated. For a fixed droplet volume, the interfacial energy per unit length of the contact line can be determined from the length of the GLI and the solid–liquid interface by

$$E(R) = \gamma b \left(\frac{\pi - 2\theta_a}{\cos\theta_a}\right) - 4\gamma \int_0^R \cos\theta_i(x)\,\mathrm{d}x, \tag{2.2}$$

where γ is the gas–liquid surface tension. Obviously, the system is at equilibrium at the stationary points/extrema of the free energy function (i.e. $\partial E/\partial R = 0$).

Here we choose β as the characteristic length to normalize the system, and the corresponding dimensionless variables are given by

$$b^* = \frac{b}{\beta}, \quad R^* = \frac{R}{\beta}, \quad V^* = \frac{V}{\beta^2}, \quad E^* = \frac{E}{\beta\gamma}. \tag{2.3a–d}$$

For simplicity, we will drop the asterisk notation in the remainder of the paper.

3. Numerical method

In recent years, the lattice Boltzmann method (LBM) has been developed into an effective and powerful computational fluid dynamics technique. It has been widely used in modelling complex multiphase flows including boiling (Chang, Huang & Lu 2017; Chang *et al.* 2019), droplet evaporation and condensation (Ledesma-Aguilar, Vella & Yeomans 2014; Hessling, Xie & Harting 2017) and the moving contact line problem (Kusumaatmaja, Hemingway & Fielding 2016). The multiphase LBM, as a diffuse-interface model, can automatically capture the GLI by incorporating two-phase interactions.

Here we implement the multicomponent multiphase (MCMP) pseudopotential lattice Boltzmann model proposed by Shan & Chen (1993) in two and three dimensions. Considering the flow system composed of two components, there are two distribution functions and each function describes the evolution of a component. Each distribution function satisfies the following lattice Boltzmann equation:

$$f_i^\sigma(\boldsymbol{x} + \boldsymbol{e}_i\Delta t, t + \Delta t) = f_i^\sigma(\boldsymbol{x}, t) - \frac{\Delta t}{\tau_\sigma}[f_i^\sigma(\boldsymbol{x}, t) - f_i^{\sigma,eq}(\boldsymbol{x}, t)], \tag{3.1}$$

where $f_i^\sigma(\boldsymbol{x}, t)$ is the density distribution function for component σ and $\boldsymbol{e}_i$ ($i = 0, 1, \ldots 8$ for 2-D cases and $i = 0, 1, \ldots 18$ for 3-D cases) are the discrete velocities. Function $f_i^{\sigma,eq}(\boldsymbol{x}, t)$ is the equilibrium distribution function. The relaxation time τ_σ is related to the kinematic viscosity as $\nu_\sigma = c_s^2(\tau_\sigma - 0.5\Delta t)$, where sound speed $c_s = c/\sqrt{3}$ and $c = \Delta x/\Delta t$. The grid spacing $\Delta x = 1$ and the time step $\Delta t = 1$. In our simulations, $\tau_\sigma = 1$, i.e. $\tau_1 = \tau_2 = 1$. Note that in the LBM, the values of physical variables are given

in lattice units. For a specific component, ρ^{maj} and ρ^{min} are the component densities at the two sides of the miscibility gap (the miscibility gap being symmetric in the model). Before simulations, we have to specify the density of the whole fluid $\rho^{maj} + \rho^{min}$, which is a constant in the whole computational domain. Here the value of $\rho^{maj} + \rho^{min}$ is chosen *a priori* as 0.736.

Using the Chapman–Enskog expansion, the lattice Boltzmann equation recovers the macroscopic governing equations, i.e. Navier–Stokes equations (Chai & Zhao 2012):

$$\frac{\partial \rho}{\partial t} + \nabla \cdot (\rho \boldsymbol{u}) = 0, \tag{3.2a}$$

$$\frac{\partial (\rho \boldsymbol{u})}{\partial t} + \nabla \cdot (\rho \boldsymbol{u}\boldsymbol{u}) = -\nabla p + \nabla \cdot [\rho \nu (\nabla \boldsymbol{u} + \nabla \boldsymbol{u}^T)] + \boldsymbol{F}, \tag{3.2b}$$

where ρ, $\boldsymbol{u}$, p and $\boldsymbol{F}$ are the mixture density, velocity, pressure and force term, respectively. Specifically, $\rho = \sum_\sigma \rho_\sigma$ and $\boldsymbol{u} = (1/\rho)(\sum_\sigma \sum_i f_i^\sigma \boldsymbol{e}_i + (1/2) \sum_\sigma \boldsymbol{F}_\sigma \Delta t)$ (Shan & Doolen 1995). Here ρ_σ is the density of component σ and $\boldsymbol{F}_\sigma$ is the force acting on component σ. The mixture viscosity $\nu = \nu_1 = \nu_2$ since τ_1 and τ_2 are identical. It should be noted that what is solved by the two-component MCMP pseudopotential lattice Boltzmann model is actually the liquid–liquid problem rather than the liquid–vapour problem. In other words, the droplet in the microchannel undergoes a dissolution/precipitation process in the surrounding liquid, which shares a common mechanism with the evaporation/condensation process of the droplet in the quasi-static limit (Xie & Harting 2019). In this mechanism, the mass change rate of the droplet is dominated by the diffusion of the droplet into the surrounding environment driven by the concentration or density gradient of droplet component in the surrounding fluid and the ambient pressure remains constant. Mathematically, these two processes are both dominated by the unsteady diffusion equation, known as Fick's second law. Since the two-component lattice Boltzmann model rather than the single-component two-phase lattice Boltzmann model (liquid–vapour model) can keep the ambient pressure constant when introducing the density gradient, we choose the former to simulate the droplet phase transitions in a microchannel.

To simulate droplet evaporation and condensation in a microchannel, the following dimensionless governing parameters are defined: the Reynolds number $Re = U_c L/\nu_1$, the capillary number $Ca = \rho^{maj} \nu_1 U_c/\gamma$, the Péclet number $Pe = U_c L/D_1$ and the Cahn number $Cn = \lambda/L$. Here, L, U_c and λ are the characteristic length, velocity and interfacial thickness, respectively. Parameter D_1 is the diffusivity of fluid 1. More basic introductions for the LBM and the detailed parameter settings are described in Appendices A.1 and A.2, respectively. The parameter settings are also introduced briefly in the following.

For a specific flow problem, simulation parameters, such as D_1, γ and λ, can be determined by specified dimensionless parameters. Suppose τ_1 is specified, then we have the viscosity of component 1 ν_1. From the definition of Re and the specified value of L, we can obtain U_c. According to the definition of Pe, we can determine the diffusivity D_1. For specific τ_1 and τ_2, D_1, σ and λ are functions of G. In addition, if $\rho^{maj} + \rho^{min}$ is given *a priori*, ρ^{maj} and ρ^{min} are also functions of G. Through D_1, the correct choice of cohesion force parameter G can be obtained (here $G = 3.6$), and then γ, λ, ρ^{maj} and ρ^{min} can all be determined (see Appendix A.2).

To impose the wetting condition on the solid surface, the surface energy formulation from the phase-field method (Fakhari & Bolster 2017) is extended to the MCMP pseudopotential lattice Boltzmann framework. This formula is able to handle complex geometric boundaries and determine the contact angle *a priori*. For the details of extending

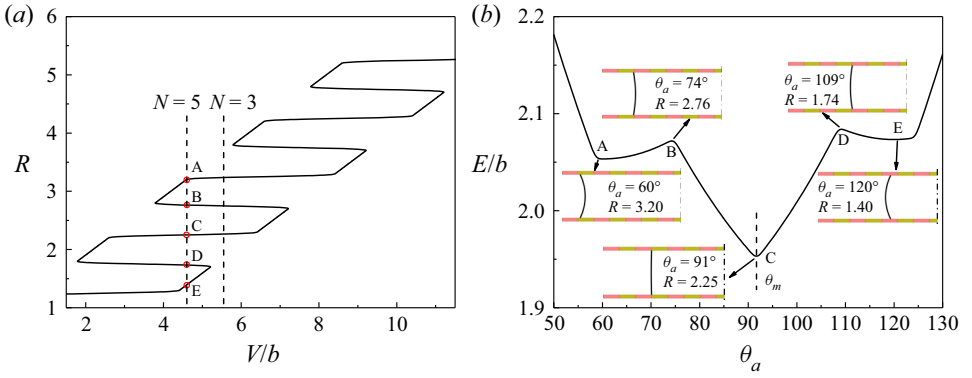

Figure 2. (*a*) Stable/metastable and unstable equilibrium configurations given by (2.1) for different droplet volumes. Here $\theta_0 = 90°$, $\varepsilon = 1.0$, $b = 10$ and $Cn = 0.108$. (*b*) Free energy as a function of the apparent contact angle for $V/b = 4.6$ (the left-hand dashed line in *a*), where θ_m is the most stable apparent contact angle. The black solid lines in the five insets show the fluid interfaces on the left-hand side of the droplet at equilibrium states. In each inset, due to symmetry, only half of the droplet is shown and the vertical dash-dotted line is the symmetric axis of the droplet. The aspect ratio is not to scale in the insets due to space limitation. If they are plotted according to $b = 10$ instead of $b \approx 2$, the droplet volumes are identical.

wetting boundary conditions to the MCMP pseudopotential LBM, refer to Appendix A.3. The numerical method is well validated in Appendix B.

Discretization errors in the computation of the cohesion force cause spurious currents around the interface. The absolute magnitude of spurious currents may be of the order 0.01 in our simulations. However, the spurious currents do not affect the evolution of the interface and the behaviour of the contact line under quasi-static circumstances. The evaporation and condensation simulations in Appendix B confirm this point.

4. Two-dimensional results and discussion

4.1. *Contact line dynamics*

We consider microchannel surfaces composed of alternating equal-width stripes of different wettabilities as shown in figure 1(*d*), which can be described by

$$\cos\theta_i(x) = \cos\theta_0 + \frac{\varepsilon}{2}\tanh[M\cos(2\pi x/\beta)], \tag{4.1}$$

where $M \to \infty$. This corresponds to the cases with a discontinuous wetting property at the junction of two types of stripes. Angle θ_0 is the reference contact angle and ε controls the strength of the chemical heterogeneity. Through the theoretical analysis described in § 2.2 combined with the local Cassie–Baxter (LCB) equation (Zhang *et al.* 2015), we can obtain all equilibrium configurations at different droplet volumes as shown in figure 2(*a*). Here the LCB equation is introduced to determine θ_a by R when the contact line is located at the junction of two types of stripes, which is expressed as

$$\cos\theta_a = f_A\cos\theta_{Ai} + f_B\cos\theta_{Bi}, \tag{4.2}$$

where θ_{Ai} and θ_{Bi} are the intrinsic contact angles of stripes A and B, respectively. Also, $f_A = l_A/\lambda$ and $f_B = l_B/\lambda$ are the thickness ratios; l_A and l_B are the thicknesses of the diffused contact line occupied by stripes A and B, respectively (see figure 3). Using the LCB equation, when R and λ are known, f_A and f_B can be calculated, and then θ_a

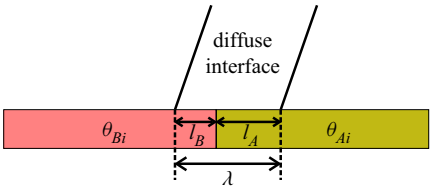

Figure 3. Schematic diagram of the calculation of apparent contact angle θ_a using the LCB equation.

is obtained. Therefore, figure 2(*a*) is generated using (2.1) and the LCB equation. Since Cn controls λ, when we plot figure 2(*a*), Cn is a relevant parameter.

It can be seen from figure 2(*a*) that for a given value of droplet volume, there is an odd number of equilibrium configurations. They represent the stable/metastable and unstable equilibrium states of the system, alternately corresponding to the minima and maxima of the free energy curve (see figure 2*b*). The outermost equilibrium configurations are stable or metastable (e.g. points A and E in figure 2*b*). Two adjacent stable/metastable states are separated by an unstable state with a free energy barrier (e.g. points A and C are separated by point B in figure 2*b*). Because of multiple equilibrium states, there are different motion trajectories of contact line as the droplet evaporates or condenses.

It is also noticed that the almost horizontal segments in figure 2(*a*) have non-zero slopes. Actually, due to our diffuse-interface model, even at the pinning stage, R is not a constant and may change slightly. More specifically, the change depends on Cn. When $Cn \to 0$ (corresponding to the macro-circumstance), since $M \to \infty$, the slope of the line segment in the pinning stage is zero.

In order to get more details of the contact line behaviour, we carry out several simulations of quasi-static evaporation/condensation of a droplet in the chemically patterned microchannel. The computational domain size is $20 \times b$. In our simulations, $\beta = 50\Delta x$, so the mesh size is $1000 \times 50b$. Initially a rectangular droplet containing fluid 1 with $\rho_1 = \rho^{maj}$ and fluid 2 with $\rho_2 = \rho^{min}$ is placed in the middle of the 2-D microchannel, and the surrounding volume consists of fluid 2 $\rho_2 = \rho^{maj}$ and fluid 1 $\rho_1 = \rho^{min}$. To drive the phase transition, a density gradient is set in the surrounding volume. For the upper and lower walls, we set the wetting condition through (A13) and set the no-slip condition. For detailed settings of boundary conditions, see Appendix A.3. Here the governing parameters are $Re = 0.003$, $Ca = 0.000025$, $Pe = 0.0042$ and $Cn = 0.108$. Values of θ_0 and ε are chosen as 90° and 1.0, respectively.

The droplet's base radius R, the apparent contact angle θ_a and the interfacial free energy E as functions of V/b for the cases of $b = 1.6$, 4 and 10 are plotted in figure 4. The results of condensation and evaporation present the advancing and receding paths of the contact line, respectively. The equilibrium configurations obtained from the theory are also shown in the figure for comparison. One can see that the advancing and receding paths follow the outermost equilibrium configurations of the system since there is no additional energy to overcome the energy barriers. Specifically, the advancing path corresponds to the outermost equilibrium configuration with a higher apparent contact angle, and the receding path corresponds to that with a lower apparent contact angle. It is worth noting that there are some critical points (e.g. points O and P in figure 4*d–f*) on the motion paths of the contact line. Saddle-node bifurcations occur at these points. Meanwhile, the outermost metastable equilibrium point coincides with the adjacent unstable equilibrium point (e.g. point O in figure 4*d–f*) and disappears immediately. Subsequently, the contact line suddenly jumps to the nearest metastable point with lower surface energy.

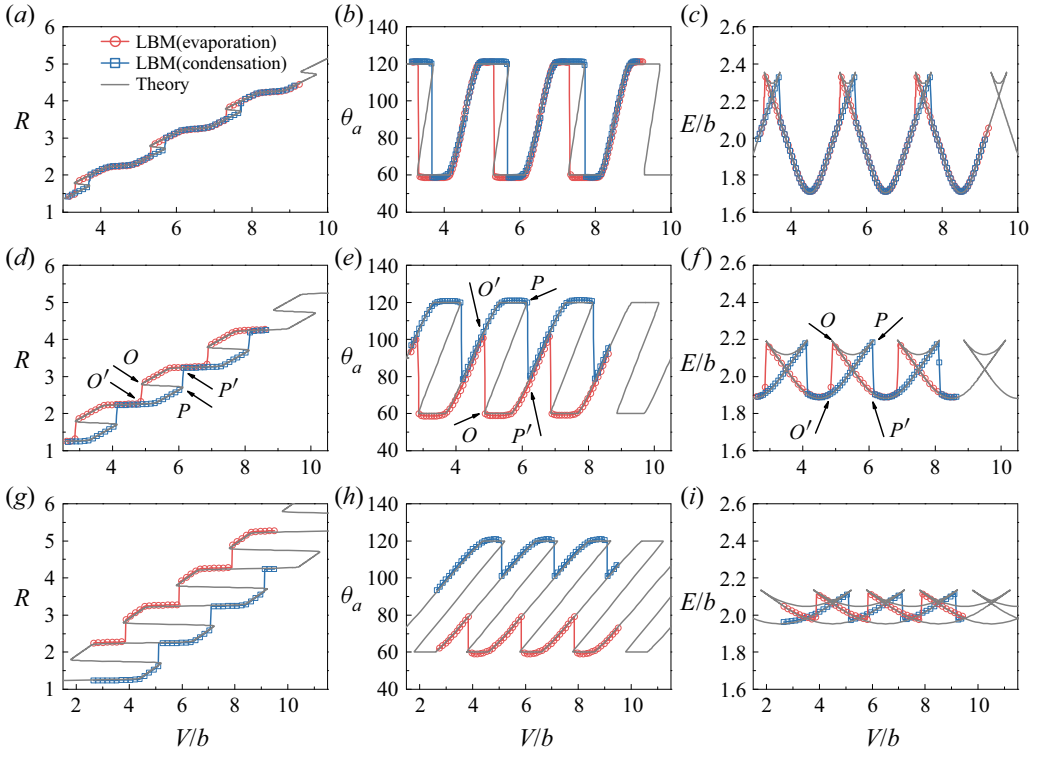

Figure 4. Comparison of CAH behaviour simulated by the LBM with that predicted by theory for cases with different b. (a,d,g) Droplet base radius R, (b,e,h) apparent contact angle θ_a and (c,f,i) system free energy E as functions of droplet volume. Cases of (a–c) $b = 1.6$, (d–f) $b = 4$ and (g–i) $b = 10$.

The excess surface energy is dissipated through capillary waves during the rapid jump (see figure 4c,f,i). It should be noted that similar effects of bifurcation diagrams have also been reported in a recent contribution on sessile droplets (Groves & Savva 2021). In general, our simulation accurately reproduces the CAH and complex contact line dynamics predicted by the theory.

In addition to jumping, other contact line behaviours, such as pinning–depinning and slip, depend entirely on the outermost equilibrium configuration varying with V, which is due to the surface chemistry. In particular, pinning–depinning occurs at the junction of two types of stripes where the wettability gradient direction is consistent with the fluid density gradient direction near the contact line. Pinning is a slowdown of the contact line dynamics dominated by the local Young's equation. When a contact line, which undergoes a slowdown stage and appears to be pinned macroscopically, completely transitions to a homogeneous part of heterogeneity, the contact line accelerates thus triggering a depinning event. All this implies that microscopic contact line pinning is not directly related to CAH, which further supports the recent result of Pradas *et al.* (2016).

The trajectories followed by apparent contact angle are shown in figure 4(b,e,h). They are two periodic fluctuating curves as observed qualitatively in experiments (Priest *et al.* 2013; Wang *et al.* 2016). The amplitude of the curves is constant, and the period $\Delta V = 2b$. One can also see that the microchannel width has a significant effect on the contact angle curves. First, when the width is small with $b = 1.6$, the contact line undergoes a slip–jump–slip–stick movement pattern (figure 5a). During the slip stage, the apparent

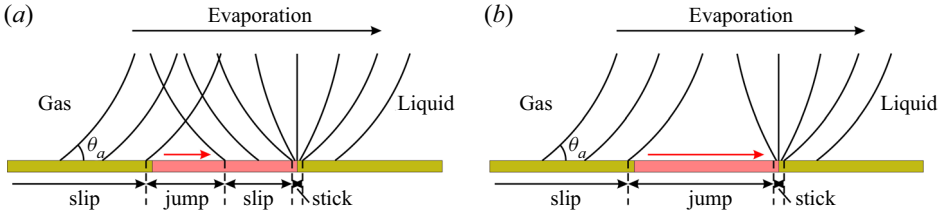

Figure 5. Schematic diagrams for motions of a droplet's left fluid interface near the wall. (*a*) Slip–jump–slip–stick and (*b*) slip–jump–stick modes. Here the evaporation process is taken as an example.

contact angle remains constant (constant contact angle mode), and during the stick stage, the droplet's base radius remains essentially constant (constant contact radius mode). During the jump process, both the apparent contact angle and the droplet's base radius undergo a sudden change. In figure 5(*a*), after the jump, the contact line moves to the adjacent stripe and continues to slip for a while until it reaches the next wettability boundary. In the stick process, the trajectories of the advancing and receding fronts coincide (see figure 4*b*), and the maximum and minimum of advancing and receding contact angles are also the same, which are equal to the inherent contact angles of the hydrophobic and hydrophilic stripes, respectively.

On increasing the microchannel width to $b = 4$, the contact line movement transforms into a slip–jump–stick mode (figure 5*b*). After the jump, the contact line directly reaches the wettability boundary and is stuck. The contact angle curves look jagged and have a smaller amplitude compared with the case of $b = 1.6$. The advancing and receding paths coincide in a certain segment of the stick stage (see figure 4*e*). On further increasing the microchannel width to $b = 10$, the contact line movement mode and the shape of contact angle curves are basically identical to those in the case of $b = 4$, except that the amplitude of contact angle curves is further reduced, and the advancing and receding paths are completely separated. Assuming $b \to \infty$, the amplitude of the contact angle curves will approach 0 and the advancing and receding contact angles remain constant, which are respectively equal to the inherent contact angles of the hydrophobic and hydrophilic stripes. This is consistent with the previous conclusion obtained from surfaces with sinusoidal heterogeneity (Hatipogullari *et al.* 2019).

Our simulations closely follow the branches in figure 4. This is a consequence of the slowness of the changes in volume V. Due to the quasi-static phase transition, the disturbance caused by the changes of V is so small that it cannot overcome the free energy barrier. However, if the phase change rate becomes faster, the significant disturbance energy caused by the change of V may overcome the free energy barrier and the jump event will occur in advance. In this circumstance, the tracing of the bifurcation curves would not be as precise.

4.2. *Equilibrium properties*

4.2.1. *The number of equilibrium configurations*

Since the CAH behaviours obtained from numerical simulation agree well with the theoretical prediction, for convenience, the data obtained from the latter are adopted in the following analysis. Before further quantitatively analysing CAH, we first pay attention to the equilibrium properties of the system. It can be seen from figure 4 that, qualitatively, the number of equilibrium configurations $N(V)$ increases with b. This is consistent with the previous conclusion obtained from a sessile droplet system (Brandon *et al.* 2003;

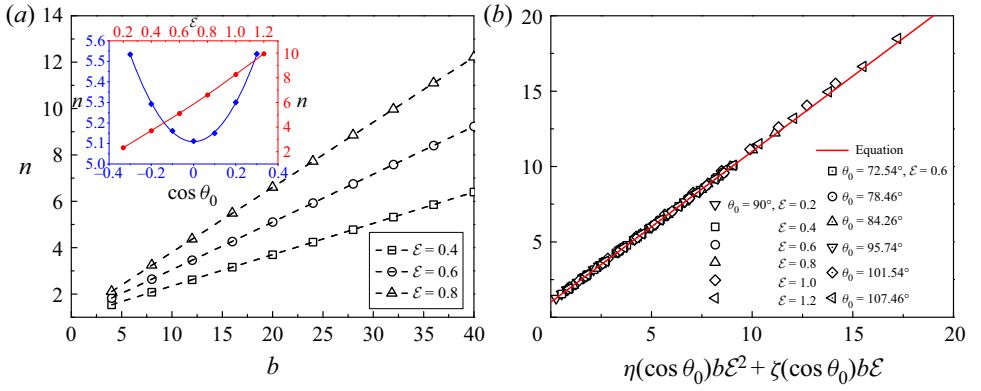

Figure 6. (*a*) Volume-averaged number of equilibrium configurations n as a function of b for different ε with $\theta_0 = 90°$. The inset shows n as a function of θ_0 and ε. (*b*) Volume-averaged number of equilibrium configurations n as a function of $\eta(\cos\theta_0)b\varepsilon^2 + \zeta(\cos\theta_0)b\varepsilon$. The red solid line is given by (4.4).

Wu *et al.* 2019). In order to quantitatively explore the influence of b on the number of equilibrium configurations, we define a volume-averaged number of equilibrium configurations in the following.

For a microchannel with width b, the number of equilibrium configurations N is a function of V. For example, figure 2(*a*) shows $N = 5$ at $V = 4.6b$, while $N = 3$ at $V = 5.5b$ when $b = 10$. Therefore N should change periodically with period $\Delta V = 2b$. In order to determine how N varies with b, we defined a volume-averaged N, i.e. the average number of equilibrium configurations in one period ΔV:

$$n = \frac{1}{\Delta V}\int_{V_i}^{V_i+\Delta V} N(V)\,\mathrm{d}V, \tag{4.3}$$

where V_i is an arbitrary value of droplet volume during phase transition. In this way, there is a determined number of equilibrium configurations for cases with a specific b.

Figure 6(*a*) shows the number n as a function of b for different heterogeneity strengths ε with $\theta_0 = 90°$. A linear dependence is found. When $b \to 0$, $n \to 1$. This means that there are no multiple equilibrium configurations and CAH. Besides b, θ_0 as well as ε also affect n. From the inset of figure 6(*a*), it can be found that the relationships between n, $\cos\theta_0$ and ε satisfy the quadratic polynomial equation. When $\varepsilon = 0$, the surfaces become homogeneous and therefore $n = 1$. In addition, the effect of θ_0 on n is symmetric about $\theta_0 = 90°$.

Based on the above observations, we suggest a model framework to comprehensively describe the effects of b, θ_0 and ε on n, which can be written as

$$n = \eta(\cos\theta_0)b\varepsilon^2 + \zeta(\cos\theta_0)b\varepsilon + 1, \tag{4.4}$$

where $\eta(\cos\theta_0)$ and $\zeta(\cos\theta_0)$ are respectively given by

$$\eta(\cos\theta_0) = a\cos^2\theta_0 + c, \quad \zeta(\cos\theta_0) = p\cos^2\theta_0 + q, \tag{4.5a,b}$$

with parameters a, c, p and q. These four parameters are constant for a specific surface chemistry and can be obtained by data fitting. As an example, for a surface composed of equal-width stripes, by fitting the data of n changing with $\cos\theta_0$ in the cases of $\varepsilon = 0.6$ and $\varepsilon = 0.8$, we obtain $a = 0.50914$, $c = 0.11071$, $p = 0.63546$ and $q = 0.65160$. In order

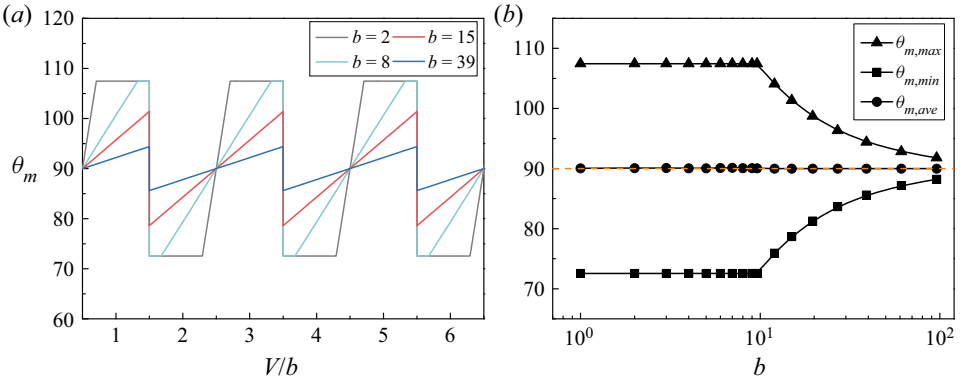

Figure 7. (*a*) The most stable contact angle θ_m as a function of V for cases with different b. (*b*) The maximum, minimum and average values of the most stable contact angle as functions of b, where the orange dashed line represents the Cassie–Baxter contact angle. Here $\theta_0 = 90^\circ$ and $\varepsilon = 0.6$.

to verify the model framework, n as a function of $\eta(\cos\theta_0)b\varepsilon^2 + \zeta(\cos\theta_0)b\varepsilon$ for various θ_0 and ε is displayed in figure 6(*b*). It is found that all the data collapse into a universal curve, which is consistent with (4.4). Therefore the proposed model framework is able to describe the influence of these three factors on n correctly and systematically.

4.2.2. *The most stable equilibrium configuration*

The most stable equilibrium configuration is the state with the global minimum of system free energy (e.g. point C in figure 2*b*), which depends on the droplet volume and is independent of the contact line's motion direction. The apparent contact angle corresponding to this configuration is the most stable contact angle θ_m. Figure 7(*a*) shows θ_m as a function of droplet volume in cases with different b. It can also be seen that b affects the most stable contact angle.

Furthermore, the variations of the maximum, minimum and average values of the most stable contact angle with b are shown in figure 7(*b*). Here the average most stable contact angle is defined as

$$\cos\theta_{m,ave} = \frac{1}{\Delta V}\int_{V_i}^{V_i+\Delta V} \cos\theta_m(V)\,\mathrm{d}V. \tag{4.6}$$

Firstly, we can see from the figure that when b is small, the maximum and minimum most stable contact angles remain constant with an increase of b. When b is larger than a critical value, they gradually decrease and increase, respectively, until they both approach the average most stable contact angle as $b \to \infty$. This means that for a limited b, the most stable contact angle may be any value in the range $[\theta_{m,min}, \theta_{m,max}]$ depending on the location of the GLI. When the microchannel is wide enough, the dependence on location disappears.

Another important piece of information obtained from figure 7(*b*) is that the average most stable contact angle remains constant with a change of b and is always equal to the contact angle predicted by the Cassie–Baxter equation (Cassie & Baxter 1944) (Cassie–Baxter contact angle):

$$\cos\theta_{CB} = \frac{1}{L_x}\int \cos\theta_i \mathrm{d}x, \tag{4.7}$$

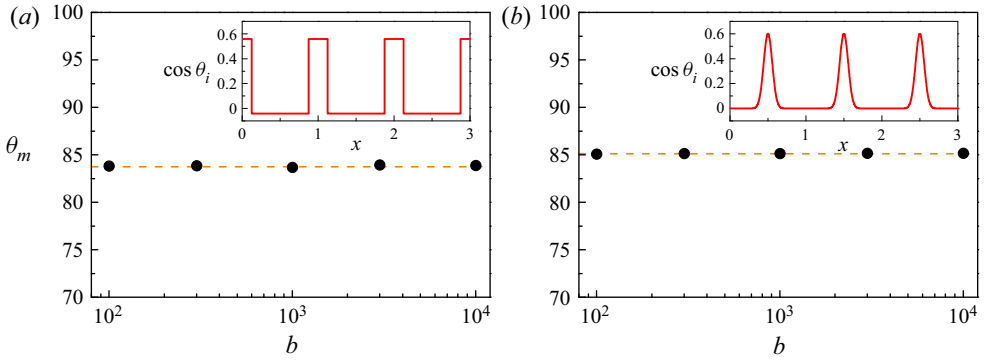

Figure 8. (*a*) The average most stable contact angle θ_m and Cassie–Baxter contact angle θ_{CB} as functions of b. The width ratio of the two types of stripes is 3 : 1 and $\theta_0 = 75^\circ$ with $\varepsilon = 0.6$. (*b*) Angles θ_m and θ_{CB} as functions of b for cases of chemically heterogeneous surfaces with Gaussian-shaped defects. The wettability distributions are shown in the insets. The filled circles and the orange dashed lines represent θ_m and θ_{CB}, respectively.

where L_x is the total microchannel length. Moreover, the identity of the average most stable contact angle and Cassie–Baxter contact angle also exists for other types of heterogeneous surfaces, e.g. surfaces with non-equal stripe widths (see the inset of figure 8*a*). Suppose the width ratio of the two types of stripes is 3 : 1, and the heterogeneities are characterized by $\theta_0 = 75^\circ$ and $\varepsilon = 0.6$. Figure 8(*a*) shows that the average most stable contact angle for different b is constant and equal to the Cassie–Baxter contact angle $\theta_{CB} = 83.75^\circ$. In addition, we also consider chemically heterogeneous surfaces with Gaussian-shaped defects (see the inset of figure 8*b*), which can be expressed as

$$\cos\theta_i(x) = \cos\theta_0 + 0.6\sum_{j=-\infty}^{\infty}\exp\left[-\frac{(x-x_j)^2}{64}\right], \tag{4.8}$$

where $x_j = 0.5 + j$. In figure 8(*b*), again, we find that the average most stable contact angle is consistent with the Cassie–Baxter contact angle for different b.

Actually, there has been much debate about the correctness of the Cassie–Baxter equation (Extrand 2003; Gao & McCarthy 2007; McHale 2007; Panchagnula & Vedantam 2007; Marmur 2009). Based on the experimental evidence, some experimentalists concluded that this equation is wrong because it cannot predict the apparent contact angle on heterogeneous surfaces (Extrand 2003; Gao & McCarthy 2007). Afterwards, theorists tried to defend this equation and explain its validity. According to the theoretical and experimental results, Marmur and others (Meiron, Marmur & Saguy 2004; Marmur 2009; Marmur & Bittoun 2009) considered that the Cassie–Baxter equation is a good approximation of the most stable contact angle if the normalized size of the GLI is large enough, i.e. L_i is much larger than β. This is consistent with our conclusion for the microchannel system. However, Gao & McCarthy (2009) disproved the view. They claimed that we should not be concerned with the normalized size of the GLI, and the Cassie–Baxter equation can and should often be used to analyse the contact angle data.

Here, based on the above discussion, we propose a new viewpoint that the Cassie–Baxter equation is a correct theory to predict the average most stable contact angle, which does not depend on the normalized size of the GLI. Therefore, the average most stable contact angle can be used as a characteristic parameter to describe the wetting properties of heterogeneous surfaces, just as Young's contact angle for homogeneous surfaces.

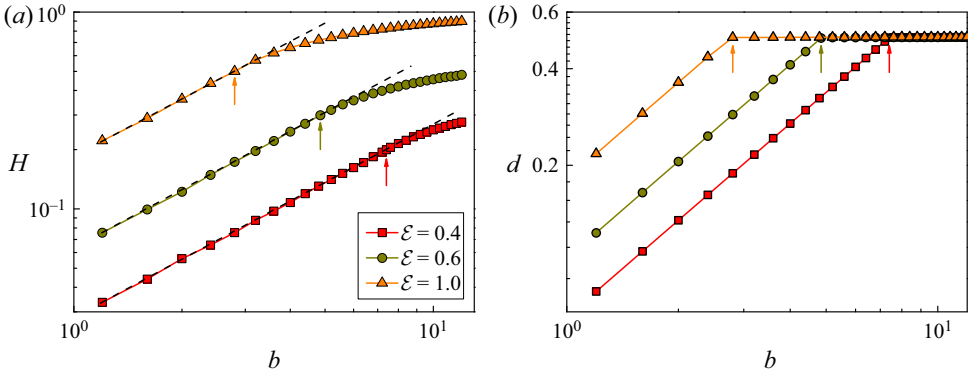

Figure 9. (*a*) Hysteresis value H and (*b*) jump distance d as functions of the microchannel width b for different heterogeneity strengths ε with $\theta_0 = 90°$. The arrows indicate the critical points. The critical microchannel widths for the cases of $\varepsilon = 0.4$, 0.6 and 1.0 are 7.4, 4.9 and 2.9, respectively.

Intuitively, for a specific heterogeneous surface, a droplet with a fixed volume will exhibit different most stable contact angles at different locations. The average most stable contact angle is the statistical average value of the most stable contact angles at each possible location, which corresponds to the global spatial-averaged characteristic of the Cassie–Baxter equation. The proposed viewpoint can also be used to explain the validity of the Wenzel equation (Wenzel 1936) on rough surfaces. It should be noted that the above conclusion is only supported by the limiting cases considered in the present work, i.e. 2-D cases with symmetry phase transitions.

4.3. *Contact angle hysteresis mode*

To find out how the microchannel width b affects the CAH, we first define the hysteresis as

$$H = \langle \cos\theta_R \rangle - \langle \cos\theta_A \rangle, \tag{4.9}$$

where $\langle \cos\theta_A \rangle = (1/\Delta V)\int_{V_i}^{V_i+\Delta V} \cos\theta_A(V)\,\mathrm{d}V$ and $\langle \cos\theta_R \rangle = (1/\Delta V)\int_{V_i}^{V_i+\Delta V} \cos\theta_R(V)\,\mathrm{d}V$. Figure 9(*a*) displays the hysteresis H as a function of b with different heterogeneity strengths. In addition, the corresponding jump distance d as a function of b is shown in figure 9(*b*). It should be noted that the jump distances in the advancing and receding paths are identical. The effect of microchannel width on the CAH can be classified into two different categories. First, when b is small, both the hysteresis H and the jumping distance d are proportional to b, i.e. $H \propto b$ and $d \propto b$. This corresponds to the slip–jump–slip–stick movement pattern of the contact line as described in § 4.1. Second, as b becomes larger than a critical value b_c, the hysteresis H would increase in a nonlinear fashion with b, and the jump distance d is almost constant. This corresponds to the slip–jump–stick pattern of contact line as mentioned in § 4.1. This piecewise linear and nonlinear behaviour of hysteresis has also been observed in previous experimental works (Di Meglio 1992). If we take the wettability of one kind of stripes as the background, the other kind of stripes can be regarded as defects. Then, the two kinds of hysteresis patterns can be considered as IDH and CDH, respectively. For the latter, CAH would be affected by two neighbouring defects close to the contact line.

The critical microchannel width b_c is dependent on θ_0 and ε; b_c as a function of θ_0 for different ε is shown in figure 10(*a*). One can see that the curves of b_c are symmetric about

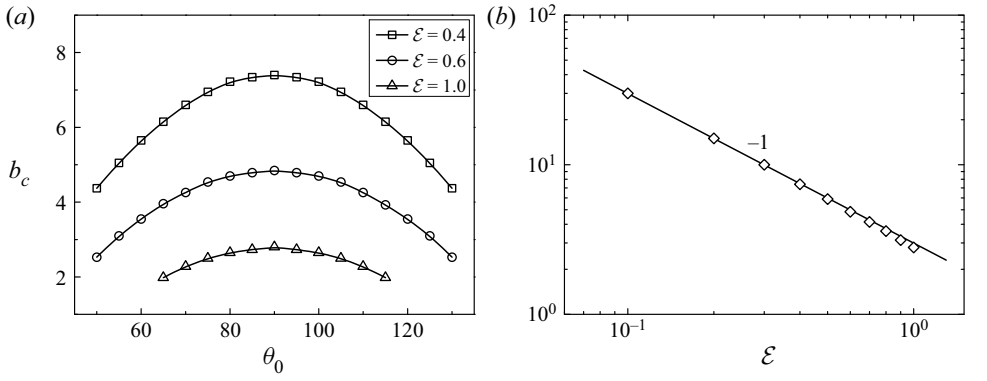

Figure 10. (*a*) Critical microchannel width b_c as a function of the reference contact angle θ_0 for different heterogeneity strengths ε. (*b*) Critical microchannel width b_c as a function of the heterogeneity strength ε for the case of $\theta_0 = 90^\circ$.

$\theta_0 = 90^\circ$ and reach peaks at that point. Critical width b_c as a function of ε with $\theta_0 = 90^\circ$ is plotted in figure 10(*b*). We find that b_c is inversely proportional to ε, i.e. $b_c \sim \varepsilon^{-1}$.

To understand the relationship between θ_0, ε and b_c, we consider the interplay between two forces, namely the defect force induced by surface heterogeneity and the elastic restoring force. Analysing the forces to study CAH was proposed by Joanny & De Gennes (1984). In our current 2-D microchannel system, there is no deformed contact line, and the elastic restoring force induced by the deformation of the GLI is dominant (Hatipogullari *et al.* 2019).

The dimensionless defect force and elastic restoring force are

$$F_d = \cos\theta_a, \tag{4.10}$$

$$F_e = k\Delta R. \tag{4.11}$$

When the system is at equilibrium, they balance each other, i.e.

$$\cos\theta_a = k\Delta R. \tag{4.12}$$

In the above equations, k is the Hookean spring coefficient and ΔR represents the deformation of the GLI and is defined as $\Delta R = R - R_s$, where R_s is the base radius of the undeformed, flat GLI of equal droplet volume. Using (2.1), (4.12) is rearranged as

$$\cos\theta_a = -kb\left[\frac{2\theta_a - \pi + \sin(2\theta_a)}{8\cos^2\theta_a}\right]. \tag{4.13}$$

Therefore, the expression of the spring coefficient is obtained, i.e.

$$k = \frac{8\cos^3\theta_a}{b[\pi - 2\theta_a - \sin(2\theta_a)]}. \tag{4.14}$$

Assuming that the heterogeneity strength ε is small, the apparent contact angle θ_a can be replaced by the constant reference contact angle θ_0 (Hatipogullari *et al.* 2019). Then we have the spring coefficient

$$k = \frac{g(\theta_0)}{b}, \tag{4.15}$$

where $g(\theta_0) = 8\cos^3\theta_0/(\pi - 2\theta_0 - \sin(2\theta_0))$ (see figure 11). In general, the spring coefficient of the interface depends not only on θ_0 but also on b. Specifically, it is inversely

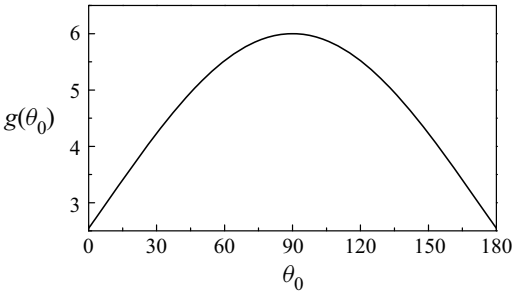

Figure 11. Plot of the function $g(\theta_0)$.

proportional to b. It is noted that in figure 11, at $\theta_0 = 90^\circ$, $g(\theta_0)$ reaches a peak. When $\theta_0 = 90^\circ$, not only the numerator but also the denominator of the $g(\theta_0)$ formula are zero and, using L'Hopital's rule, we have $g(90^\circ) = 6$.

The force balance (4.12) leads to a simple graphical construction as shown in figure 12. We pay attention to the elastic restoring force curve (i.e. the black dashed line). First, it can be seen from the figure that, for fixed θ_0 and ε, the slope of the curve decreases with an increase of b. When the droplet evaporates or condenses, the elastic restoring force curve shifts to the left or right, respectively. The intersections of the elastic restoring force and the defect force curves represent the equilibrium configurations of the system. Next, when the elastic restoring force curve coincides with the point where saddle-node bifurcation occurs, jumping behaviour is induced (red and green lines in the figure). The IDH and CDH correspond to the cases shown in figures 12(a) and 12(c), respectively, while figure 12(b) represents the critical state of the two hysteresis modes. From the geometric plot, we have the critical condition

$$k_c = \frac{g(\theta_0)}{b_c} = 2\varepsilon. \tag{4.16}$$

Hence, the critical microchannel width is

$$b_c = \frac{g(\theta_0)}{2\varepsilon}. \tag{4.17}$$

This formula is consistent with the symmetry shown in figure 10(a) and the scaling behaviour shown in figure 10(b).

4.4. *Scaling laws analysis of CAH*

According to Joanny & De Gennes (1984), the influence of each defect on the contact line behaviour is assumed to be independent (i.e. IDH). Based on this assumption, the relationship between the hysteresis and the dissipated energy for a dilute system of defects is derived as (Joanny & De Gennes 1984)

$$H = \phi W, \tag{4.18}$$

where ϕ is the defect density (the number of defects per unit area) and W is the dissipated energy per defect in a hysteresis cycle. Then the scaling law (1.1) was established through (4.18). However, for CDH, this scaling law no longer holds. In this section, we extend the model of Joanny and de Gennes to the CDH cases, and a scaling law for the two hysteresis modes can be well established.

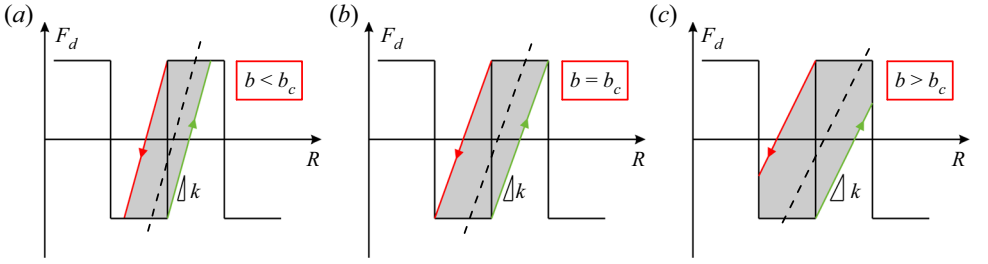

Figure 12. Graphical construction of the force balance on surfaces with alternating equal-width stripes of different wettabilities with reference contact angle $\theta_0 = 90^\circ$ for cases (*a*) $b < b_c$, (*b*) $b = b_c$ and (*c*) $b > b_c$. The black solid lines and dashed lines represent the defect force and the elastic restoring force, respectively, and their intersections represent the equilibrium configurations of the system. The red and green solid lines indicate the jumping behaviour of the contact line in the receding and advancing directions, respectively. The grey areas represent the dissipated energy in a hysteresis cycle.

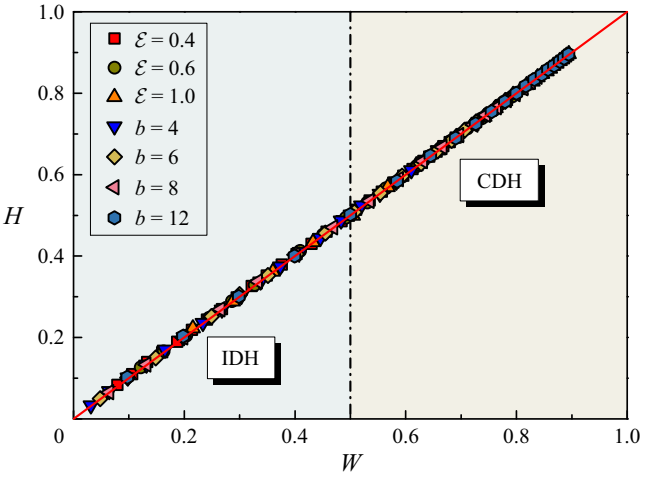

Figure 13. Hysteresis H as a function of dissipated energy in a hysteresis cycle W for different b at several fixed ε and for different ε at several fixed b.

To this end, we first examine the relationship between H and W for both the IDH and CDH cases in the current microchannel system. Figure 13 shows H as a function of W for different b at several fixed ε and for different ε at several fixed b. It can be seen that (4.18) is satisfied for both the IDH and CDH cases (here $\phi \equiv 1$). This is reasonable since surface heterogeneity is periodic. Therefore (4.18) does not depend on the hysteresis mode.

Actually, W is equal to the shaded area in the force balance graphical construction (figure 12). For the microchannel that we studied, the shaded area is a parallelogram (figure 12*a*) and a parallel hexagon (figure 12*c*) for IDH and CDH, respectively. By calculating their area and using (4.18), the hysteresis of the IDH and CDH modes can be obtained as

$$H = \frac{b\varepsilon^2}{g(\theta_0)} \tag{4.19a}$$

and

$$H = \varepsilon - \frac{g(\theta_0)}{4b}, \tag{4.19b}$$

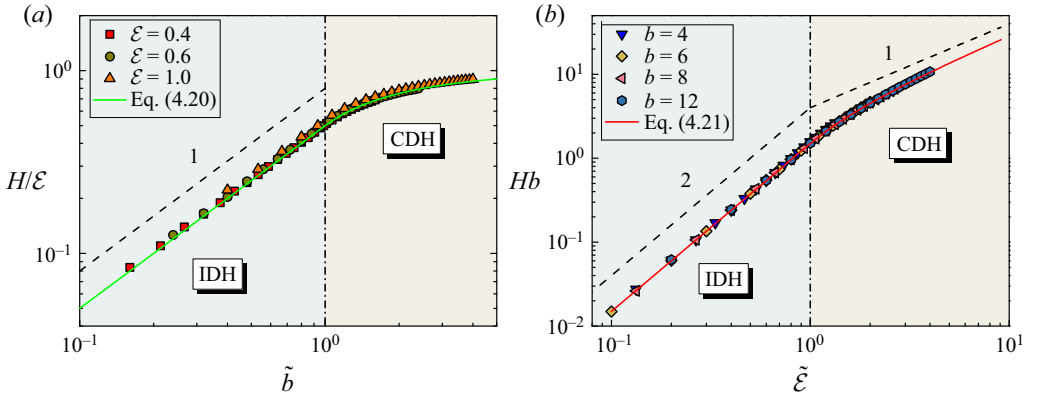

Figure 14. (*a*) Rescaled hysteresis H/ε as a function of $\tilde{b}$ for different ε. (*b*) Plot of Hb as a function of $\tilde{\varepsilon}$ for different b.

respectively. It is seen that the formulas are quite different. For IDH, H is proportional to $b\varepsilon^2$. However, for CDH, H is linearly dependent on ε. In addition, with an increase of b, H increases nonlinearly and finally approaches a constant ε.

Next, we check the correctness of (4.19*a*) and (4.19*b*). Rescaling H and b with ε and b_c, respectively, we have

$$\frac{H}{\varepsilon} = \begin{cases} \dfrac{\tilde{b}}{2}, & \tilde{b} \leqslant 1 \\ 1 - \dfrac{1}{2\tilde{b}}, & \tilde{b} > 1, \end{cases} \tag{4.20}$$

where $\tilde{b} = b/b_c$. Figure 14(*a*) shows the rescaled hysteresis H/ε as a function of $\tilde{b}$. It can be seen that H/ε for different ε collapses into a single curve, which is accurately predicted by (4.20). On the other hand, we also investigate the effect of heterogeneity strength on H. Adopting $1/b$ and ε_c to rescale H and ε, respectively, we obtain

$$Hb = \begin{cases} \dfrac{g(\theta_0)\tilde{\varepsilon}^2}{4}, & \tilde{\varepsilon} \leqslant 1 \\ \dfrac{g(\theta_0)}{4}(2\tilde{\varepsilon} - 1), & \tilde{\varepsilon} > 1, \end{cases} \tag{4.21}$$

where $\tilde{\varepsilon} = \varepsilon/\varepsilon_c$. Figure 14(*b*) shows Hb as a function of $\tilde{\varepsilon}$. It can be seen that all data for different b collapse into a single curve, which is consistent with the prediction, i.e. (4.21). The quadratic dependence and the linear dependence on $\tilde{\varepsilon}$ are observed in the IDH and CDH regions, respectively.

5. Three-dimensional results

In this section, the CAH in a 3-D chemically heterogeneous microchannel is numerically studied using the LBM. We consider neutral wetting surfaces ($\theta_i = 90^\circ$) with regularly arranged circular hydrophilic defects ($\theta_i = 45^\circ$). The dimensionless radii of circular defects are $r = 0.25$. Here β is also the characteristic length and the contact angle of the neutral wetting surfaces is regarded as the reference contact angle, i.e. $\theta_0 = 90^\circ$. The initial droplet is symmetrically placed in the microchannel, and the centre of the droplet

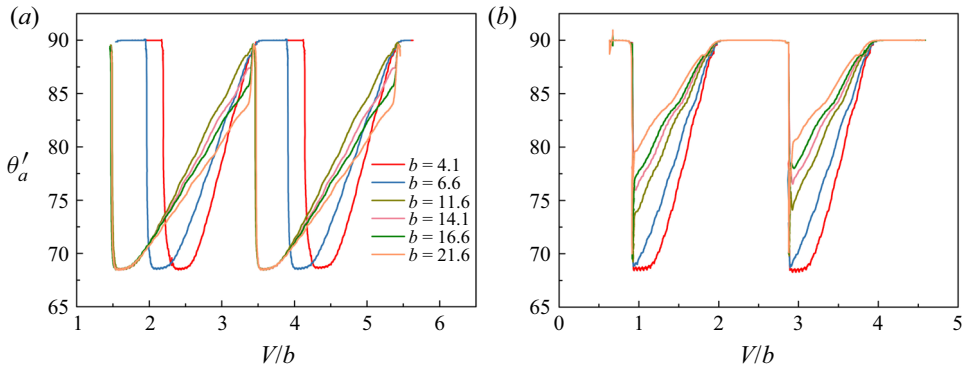

Figure 15. The average apparent contact angle θ_a' as a function of V during (a) evaporation and (b) condensation for cases with different b.

corresponds to the neutral wetting region of the wall (see figure 1c). In the 3-D simulations, the computational domain of the microchannel is $L_x \times L_y \times L_z = 7 \times 1 \times b$. The grid spacing is $\Delta x = \frac{1}{48}\beta$ and the corresponding mesh size is $336 \times 48 \times 48b$. The front and rear boundaries are periodic. Constant density is imposed on the left and right boundaries to drive the quasi-static evaporation or condensation of the droplet. For more details of phase transition settings, see § 4.1.

In the 3-D cases, for a specific contact line shape, the local apparent contact angle is space-dependent in the y direction, i.e. $\theta_a = \theta_a(y)$. The spatially averaged apparent contact angle is

$$\theta_a' = \int_0^1 \theta_a(y)\,\mathrm{d}y. \tag{5.1}$$

Similarly, the spatially averaged base radius can be calculated as

$$R' = \int_0^1 R(y)\,\mathrm{d}y. \tag{5.2}$$

Figures 15(a) and 15(b) show θ_a' as a function of V during evaporation and condensation, which are the spatially averaged receding contact angle θ_R' and advancing contact angle θ_A', respectively. It can be seen that for evaporation (figure 15a), when $b \leqslant b_c$, where $b_c \approx 11.6$, θ_a', i.e. θ_R', is maintained at 90° for a while (there is a plateau). However, when $b \geqslant b_c$, the evolution trend of θ_R' becomes different because there is no such plateau. For condensation (figure 15b), the evolution trend of θ_a', i.e. θ_A', is identical in all cases and not affected by b. The curves of θ_R' for small and large microchannel widths correspond to the slip–jump–slip–stick (IDH) and slip–jump–stick (CDH) movement modes of the contact line, respectively. Similar to the 2-D cases, the CAH is defined as $H = \langle\cos\theta_R'\rangle - \langle\cos\theta_A'\rangle$, where $\langle\cos\theta_R'\rangle = (1/\Delta V)\int_{V_i}^{V_i+\Delta V}\cos\theta_R'(V)\,\mathrm{d}V$ and $\langle\cos\theta_A'\rangle = (1/\Delta V)\int_{V_i}^{V_i+\Delta V}\cos\theta_A'(V)\,\mathrm{d}V$.

During the quasi-static phase transition, both R' and θ_a' are uniquely determined by the droplet volume and the deformation of the contact line. Actually, we find that θ_a' is a single-valued function of R'. The details are illustrated in the following.

For the droplet's phase transition in the 3-D heterogeneous microchannel studied here, the deformation of the contact line may be affected by: phase transition time, b and phase transition type (i.e. evaporation or condensation). For the specified phase transition type

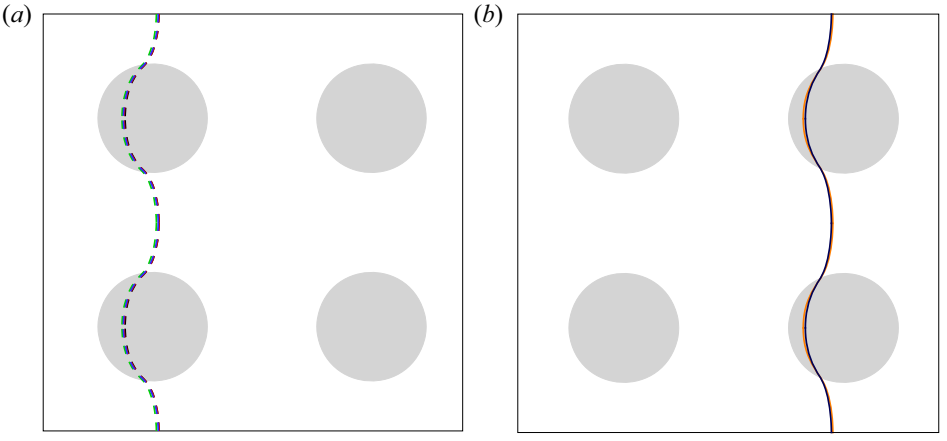

Figure 16. (*a*) Deformed contact line during droplet evaporation for different b with $R' = 1.56$, where the black, blue, green and red dashed lines represent the cases of $b = 6.6$, 11.6, 16.6 and 21.6, respectively. (*b*) Deformed contact line in the process of droplet evaporation and condensation with $b = 1.6$ and $R' = 0.61$, where the orange and blue solid lines represent the cases of evaporation and condensation, respectively.

and b, phase transition time is a single-valued function of R'. Therefore, the deformation of the contact line may be affected by R', b and phase transition type. However, through the numerical simulation results, we found that the deformation of the contact line does not depend on b and phase transition type. We illustrate this in figure 16.

Figure 16(*a*) shows the deformed contact line during droplet evaporation for different b with $R' = 1.56$. It can be seen that the contact lines for different b coincide, indicating that the deformation of the contact line does not depend on b. Figure 16(*b*) shows a comparison of the deformed contact line during droplet evaporation and condensation with $b = 1.6$ and $R' = 0.61$. It seems that the deformation is not relevant to the type of phase transition. Therefore during the movement of the contact line, the deformation of the contact line can be uniquely determined by R'. Actually, under the assumption of quasi-static phase transition, the local apparent contact angle is determined by the local capillary force balance, which is related to the surface chemical properties. So θ_a' can be uniquely determined by the deformation of the contact line. In other words, θ_a' is a single-valued function of R'.

Since θ_a' is a single-valued function of R', the 3-D problem can be transformed into a 2-D problem similar to that in § 4. In the 3-D cases, due to the deformation of the contact line, the distribution of defect force cannot be given directly according to the surface wettability. Since the microchannel width does not influence the deformation of the contact line, by simulating the droplet phase transition in the case of small b, e.g. $b = 0.4$ (the hysteresis is negligible), we obtain the average defect force F_d' ($F_d' = \cos\theta_a'$) as a function of R', and the result is shown in figure 17(*a*). The small oscillations at the peak of the curve in this figure may be attributed to the polygonal approximation of circular defects in the wall mesh. When the resolution is sufficient, the oscillations will disappear.

It can be seen that the defect force curve is close to a Gaussian-shaped distribution. Under the assumption of local defects (defect size r is much smaller than the spatial period of surface heterogeneity, i.e. $r/\beta \ll 1$), the shaded area can be calculated by approximating it as a triangle (Joanny & De Gennes 1984; Delmas *et al.* 2011; Lhermerout & Davitt 2018), while that in the case of CDH can be calculated by approximating it as a trapezoid. However, in our simulations, the assumption of local defects is not satisfied.

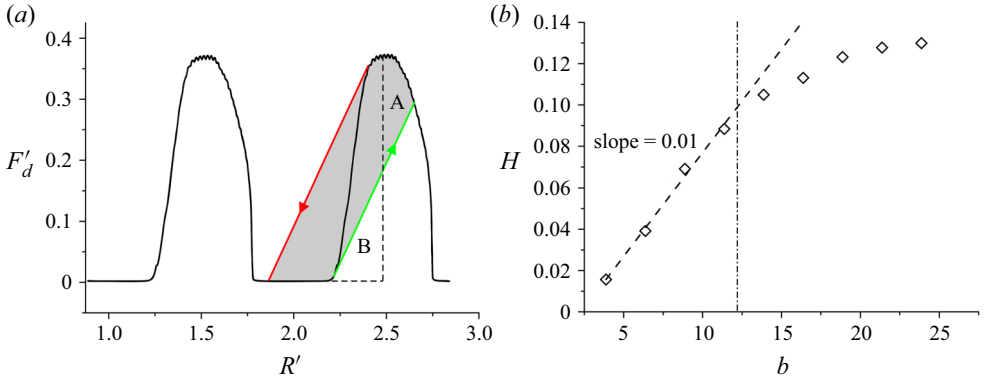

Figure 17. (*a*) Graphical construction of force balance on 3-D chemically heterogeneous surfaces for IDH. The black solid line represents the defect force. (*b*) Hysteresis H as a function of b in the 3-D chemically heterogeneous microchannel. The dashed line is the fitting line of linear stage, and the dash-dotted line represents $b = 12.2$.

So it is difficult to perform a quantitative analysis on the correlation between CAH and b. However, in the IDH mode, if the areas of A and B in figure 17(*a*) are assumed to be equal, the area of the shaded part can be converted to that of a triangle, which is composed of the red line and the dashed lines. In this way, from the geometric plot, we have $H = 0.5b\varepsilon'^2/g(\theta_0)$ (ε' refers to the maximum value of F'_d and $\varepsilon' \approx 0.37$ here). It seems that H increases linearly with b in the IDH mode. The formula is confirmed by our numerical results (see figure 17*b*). Figure 17(*b*) shows that when b is small the linear data fitting is $H = 0.01b$. The slope is consistent with the analytical value $0.5\varepsilon'^2/g(\theta_0) \approx 0.011$.

On the other hand, when b is large, we can see a nonlinear relationship between H and b, which corresponds to the 3-D CDH mode. According to figure 17(*a*), we have a critical microchannel width to distinguish the two hysteresis patterns, $b_c = 12.2$, which can also be seen in figure 17(*b*). The above discussions of the 3-D cases demonstrate that the theoretical results of 2-D cases (§ 4) can be well extended to 3-D cases.

6. Conclusions

Through theoretical analysis and numerical simulation based on the diffuse-interface LBM, the CAH in a heterogeneous microchannel is systematically studied.

Our numerical simulations accurately reproduce the CAH and complex contact line dynamics predicted by the theory. The contact line behaviours depend on the change of outermost equilibrium configurations with volume in the quasi-static regime. The contact line would jump at some critical points where saddle-node bifurcations occur.

The microchannel width effect on the system's equilibrium properties is considered. The volume-averaged number of equilibrium configurations n is found to be linearly dependent on the microchannel width b, and further it can be written as $n = \eta(\cos\theta_0)b\varepsilon^2 + \zeta(\cos\theta_0)b\varepsilon + 1$. The average most stable contact angle does not depend on b and is always equal to the contact angle predicted by the Cassie–Baxter equation.

Two different hysteresis regimes, i.e. IDH and CDH, are identified for small and large b, respectively. The critical microchannel width b_c separating the two hysteresis regimes is a function of the reference contact angle θ_0 and the heterogeneity strength ε. In particular,

b_c is inversely proportional to ε, i.e. $b_c \sim \varepsilon^{-1}$. A graphical force balance approach is constructed to understand the correlation between θ_0, ε and b_c.

Finally, based on the graphical construction of the force balance, a scaling law is established for the hysteresis value H, which is a function of b and ε. In the IDH mode, $H \sim b\varepsilon^2$, while in the CDH mode, H increases linearly with ε but nonlinearly with b. We also demonstrated that some of the conclusions for the 2-D case can be well extended to the 3-D case.

Funding. This work was supported by the Natural Science Foundation of China (NSFC) (grant nos. 11772326 and 11472269) and the Joint Funds of the National Natural Science Foundation of China (grant no. U21B2070).

Declaration of interests. The authors report no conflict of interest.

Author ORCIDs.
Xiangting Chang https://orcid.org/0000-0002-4162-8131;
Haibo Huang https://orcid.org/0000-0002-1308-9900;
Xi-Yun Lu https://orcid.org/0000-0002-0737-6460.

Appendix A. The MCMP pseudopotential LBM

A.1. *Basic formulation*

In our study, there are two components and the evolution equation of the density distribution function (3.1) is applicable not only to component 1 but also to component 2. The equilibrium distribution function $f_i^{\sigma,eq}(\boldsymbol{x}, t)$ can be calculated as (Huang, Sukop & Lu 2015)

$$f_i^{\sigma,eq}(\boldsymbol{x}, t) = \omega_i \rho_\sigma \left[1 + \frac{\boldsymbol{e}_i \cdot \boldsymbol{u}_\sigma^{eq}}{c_s^2} + \frac{(\boldsymbol{e}_i \cdot \boldsymbol{u}_\sigma^{eq})^2}{2c_s^4} - \frac{(\boldsymbol{u}_\sigma^{eq})^2}{2c_s^2}\right]. \tag{A1}$$

For the D2Q9 (two dimensional nine velocities) and D3Q19 (three dimensional nineteen velocities) models used here, the discrete velocities $\boldsymbol{e}_i$ are given by

$$[\boldsymbol{e}_0, \boldsymbol{e}_1, \boldsymbol{e}_2, \boldsymbol{e}_3, \boldsymbol{e}_4, \boldsymbol{e}_5, \boldsymbol{e}_6, \boldsymbol{e}_7, \boldsymbol{e}_8] = c\begin{bmatrix} 0 & 1 & 0 & -1 & 0 & 1 & -1 & -1 & 1 \\ 0 & 0 & 1 & 0 & -1 & 1 & 1 & -1 & -1 \end{bmatrix} \tag{A2}$$

and

$$[\boldsymbol{e}_0, \boldsymbol{e}_1, \boldsymbol{e}_2, \boldsymbol{e}_3, \boldsymbol{e}_4, \boldsymbol{e}_5, \boldsymbol{e}_6, \boldsymbol{e}_7, \boldsymbol{e}_8, \boldsymbol{e}_9, \boldsymbol{e}_{10}, \boldsymbol{e}_{11}, \boldsymbol{e}_{12}, \boldsymbol{e}_{13}, \boldsymbol{e}_{14}, \boldsymbol{e}_{15}, \boldsymbol{e}_{16}, \boldsymbol{e}_{17}, \boldsymbol{e}_{18}]$$
$$= c\begin{bmatrix} 0 & 1 & -1 & 0 & 0 & 0 & 0 & 1 & -1 & 1 & -1 & 1 & -1 & 1 & -1 & 0 & 0 & 0 & 0 \\ 0 & 0 & 0 & 1 & -1 & 0 & 0 & 1 & 1 & -1 & -1 & 0 & 0 & 0 & 0 & 1 & -1 & 1 & -1 \\ 0 & 0 & 0 & 0 & 0 & 1 & -1 & 0 & 0 & 0 & 0 & 1 & 1 & -1 & -1 & 1 & 1 & -1 & -1 \end{bmatrix}, \tag{A3}$$

respectively. For the D2Q9 model, the corresponding weighting coefficients ω_i are given by $\omega_i = \frac{4}{9}$ for $i = 0$, $\omega_i = \frac{1}{9}$ for $i = 1, \ldots, 4$ and $\omega_i = \frac{1}{36}$ for $i = 5, \ldots, 8$. For the D3Q19 model, ω_i are $\omega_i = \frac{1}{3}$ for $i = 0$, $\omega_i = \frac{1}{18}$ for $i = 1, \ldots, 6$ and $\omega_i = \frac{1}{36}$ for $i = 7, \ldots, 18$.

The density and macroscopic velocity of component σ can be obtained through (Shan & Chen 1993)

$$\rho_\sigma = \sum_i f_i^\sigma \tag{A4}$$

and

$$\boldsymbol{u}_\sigma^{eq} = \boldsymbol{u}' + \frac{\tau_\sigma \boldsymbol{F}_\sigma}{\rho_\sigma}, \tag{A5}$$

respectively, where $\boldsymbol{u}'$ is the velocity of the whole fluid and is defined as

$$\boldsymbol{u}' = \frac{\sum_\sigma \left(\sum_i \frac{f_i^\sigma \boldsymbol{e}_i}{\tau_\sigma} \right)}{\sum_\sigma \frac{\rho_\sigma}{\tau_\sigma}}. \tag{A6}$$

In the present work, the force term only involves the pseudopotential cohesive force that induces the separation of the components. The force acting on component σ is (Hessling *et al.* 2017)

$$\boldsymbol{F}_\sigma(\boldsymbol{x}, t) = -G\psi_\sigma(\boldsymbol{x}, t) \sum_i \omega_i \psi_{\bar{\sigma}}(\boldsymbol{x} + \boldsymbol{e}_i \Delta t, t) \boldsymbol{e}_i, \tag{A7}$$

where σ and $\bar{\sigma}$ denote two different fluid components. If σ denotes component 1, $\bar{\sigma}$ denotes component 2. The parameter G controls the strength of the cohesion force and there is a threshold value G_c. Only when $G > G_c$ will an initially uniform mixed system of two immiscible fluids yield a stable separation (Huang *et al.* 2015). In this circumstance, we can simulate immiscible two-component flows. More discussion of parameters G and G_c can be found in Huang *et al.* (2015). The interparticle potential $\psi_\sigma(\boldsymbol{x}, t)$ is defined as $\psi_\sigma(\boldsymbol{x}, t) = \rho_0[1 - \mathrm{e}^{-\rho_\sigma(\boldsymbol{x},t)/\rho_0}]$, where ρ_0 is a constant and chosen as 1 (Shan & Chen 1993).

A.2. *Determination of simulation parameters*

In the definitions of dimensionless parameters, the characteristic length L differs in different flow problems. For the cases of droplet phase transition inside a heterogeneous microchannel, $L = \beta$. The characteristic velocity U_c can be defined as follows. For the diffusion-dominated droplet phase transition, when droplet's base radius is much smaller than half the length of the microchannel, i.e. $R \ll R_b$, the influence of contact angle on phase transition rate can be neglected. Then the rate of change of droplet volume V is (Popov 2005)

$$\frac{\mathrm{d}V}{\mathrm{d}t} = -\frac{bD_1\delta}{\rho^{maj}(R_b - R)}. \tag{A8}$$

Integrating (A8), one can get the quasi-static diffusion-dominated evaporation/condensation model:

$$(V - V_0)(2bR_b - V - V_0) = -\frac{2b^2 D_1 \delta}{\rho^{maj}} t, \tag{A9}$$

where V_0 is the initial droplet volume. Defining the characteristic velocity U_c as the average moving velocity of the contact line in the phase transition process, according to

(A9), we have

$$U_c = \frac{D_1 \delta}{2(R_b - R_0)\rho^{maj}}. \tag{A10}$$

It can be seen that, indeed, U_c is a linear function of δ. Here D_σ is related to the lattice Boltzmann parameters through (Hessling *et al.* 2017)

$$D_\sigma = c_s^2(\tau_\sigma - 0.5\Delta t) - \frac{Gc_s^2}{\rho_\sigma + \rho_{\bar{\sigma}}}(\rho_{\bar{\sigma}}\psi_\sigma\psi'_{\bar{\sigma}} + \rho_\sigma\psi_{\bar{\sigma}}\psi'_\sigma), \tag{A11}$$

where $\psi'_\sigma = \mathrm{d}\psi_\sigma/\mathrm{d}\rho_\sigma$ (Shan & Doolen 1995). Parameter λ is the interfacial thickness. In the MCMP pseudopotential LBM, λ can be measured from the simulations. If the region $1.05\rho^{min} < \rho_1 < 0.95\rho^{maj}$ is regarded as an interfacial region, by measuring the width of the region, λ can be obtained. In the LBM, given the value of τ_σ, ρ^{maj}, ρ^{min}, λ, γ and D_σ are determined via G. In our simulations, $\tau_1 = \tau_2 = 1$. The value of G is chosen as $G = 3.6$ according to Hessling *et al.* (2017). Then we have $\rho^{maj} = 0.7$, $\rho^{min} = 0.036$, $\lambda = 5.4$, $\gamma = 0.047$ and $D_1 = D_2 = 0.12$. The non-equilibrium density mismatch is set to $\delta = 0.011$.

Next, we illustrate how to obtain the dimensional simulation parameters such as diffusivity D_1, surface tension γ and δ in the LBM through the specified non-dimensional parameters.

First, suppose $\tau_1 = \tau_2 = 1$ is specified, then we have the viscosity of component 1, $\nu_1 = 0.17$. Since L has been specified, from the definition of Reynolds number, i.e. $Re = U_c L/\nu_1$, we can obtain U_c.

Second, according to the definition of Péclet number (Pe), i.e. $Pe = U_c L/D_1$, we can determine the diffusivity D_1.

Third, as $\tau_1 = \tau_2 = 1$ is fixed, diffusivity D_1 is only a function of G (see (A11)). According to D_1 and the function, we can obtain the correct choice of G. After G is determined, the surface tension γ, interfacial thickness λ, ρ^{maj} and ρ^{min} can all be determined.

Finally, through (A10), δ can be obtained. Then before we perform our simulation, we can specify the imposed non-equilibrium density mismatch (δ), which is the driving factor of the phase transition process.

A.3. *Boundary conditions*

In order to calculate the cohesive force of the fluid nodes near the solid boundary ($\boldsymbol{x}_b$ in figure 18) using (A7), we need to know the density values of wall nodes ($\boldsymbol{x}_s$), which can be obtained by the wetting boundary condition.

To impose the wetting boundary condition on the solid wall, the order parameter is first defined as

$$\varphi_\sigma(\boldsymbol{x}) = \frac{\rho_\sigma(\boldsymbol{x}) - \rho^{min}}{\rho^{maj} - \rho^{min}}. \tag{A12}$$

Using the finite difference method to discretize the derivative, then the wetting condition is expressed as

$$\boldsymbol{n}_w \cdot \nabla\varphi_\sigma\,|_{\boldsymbol{x}_w} = \frac{\varphi_\sigma(\boldsymbol{x}_b) - \varphi_\sigma(\boldsymbol{x}_s)}{s + h} = -\frac{4}{\lambda}\Theta\varphi_\sigma(\boldsymbol{x}_w)[1 - \varphi_\sigma(\boldsymbol{x}_w)], \tag{A13}$$

where $\boldsymbol{n}_w$ is the unit vector normal to the solid wall and $\varphi_\sigma(\boldsymbol{x}_w)$ is the order parameter value at wall point $\boldsymbol{x}_w$. Angle Θ is related to the specified intrinsic contact angle measured

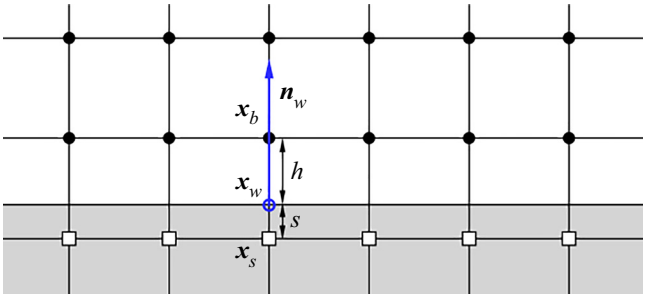

Figure 18. Schematic diagram for the implementation of condition (A13). The shaded region denotes the solid region.

in fluid σ as $\Theta = \cos\theta_i$ for component σ and $\Theta = \cos(\pi - \theta_i)$ for component $\bar{\sigma}$. Here $s = |\boldsymbol{x}_w - \boldsymbol{x}_s|$. Parameter h is the distance between the wall point $\boldsymbol{x}_w$ and the boundary node $\boldsymbol{x}_b$ (see the schematic diagram in figure 18).

The order parameter at wall point $\boldsymbol{x}_w$ can be obtained through

$$\varphi_\sigma(\boldsymbol{x}_w) = \frac{h\varphi_\sigma(\boldsymbol{x}_s) + s\varphi_\sigma(\boldsymbol{x}_b)}{s+h}. \tag{A14}$$

Substituting (A14) into (A13), we have

$$\varphi_\sigma(\boldsymbol{x}_s) = \begin{cases} \dfrac{s+h}{2hm}[1+m-\sqrt{(1+m)^2-4m\varphi_\sigma(\boldsymbol{x}_b)}] - \dfrac{s}{h}\varphi_\sigma(\boldsymbol{x}_b), & \theta_i \neq 90^\circ \\ \varphi_\sigma(\boldsymbol{x}_b), & \theta_i = 90^\circ, \end{cases} \tag{A15}$$

where $m = -(4h/\lambda)\Theta$. Once $\varphi_\sigma(\boldsymbol{x}_s)$ is known, $\rho_\sigma(\boldsymbol{x}_s)$ can be obtained according to (A12). Then the cohesive force on the boundary nodes $\boldsymbol{x}_b$ can be calculated using (A7). In the present work, h and s are chosen as $h = s = 0.5$.

In our simulations, to drive the droplet phase transition in the microchannel, a density gradient is set in the surrounding volume by imposing a constant density $\rho_1 = \rho^{min} - \delta$ and a zero velocity on the left and right boundaries. Meanwhile $\rho_2 = \rho^{maj} + \delta$ is set on these boundaries to eliminate the pressure gradient, where δ is a small quantity. Evaporation and condensation occur when $\delta > 0$ and $\delta < 0$, respectively. For the upper and lower walls, we set the wetting condition (A13) and set the no-slip condition through the half-way bounce-back scheme of f_i^σ (Ziegler 1993). For the initial condition and the left and right boundary conditions, f_i^σ in the fluid domain can be obtained according to the macroscale density and velocity. Generally, when macroscale variables ρ_σ and velocity are specified, we can set f_i^σ equal to its equilibrium value $f_i^{\sigma,eq}$.

Appendix B. Validation

We first validate the extended contact angle model by using a benchmark problem of droplet wetting/dewetting on a flat surface. The 2-D rectangular computational domain Ω is bounded by the top and bottom walls. The periodic boundary condition is imposed in the horizontal direction. Initially, a semicircular droplet with a contact angle of 90° and radius of R_0 is placed on the bottom surface. Here R_0 is the characteristic length. The dimensions of the domain are $[0, 8] \times [0, 4]$, and the corresponding mesh size is 401×201. When different wettability is specified, the droplet will spread or recoil, until reaching an equilibrium state (figure 19*a–c*). We perform several simulations on surfaces

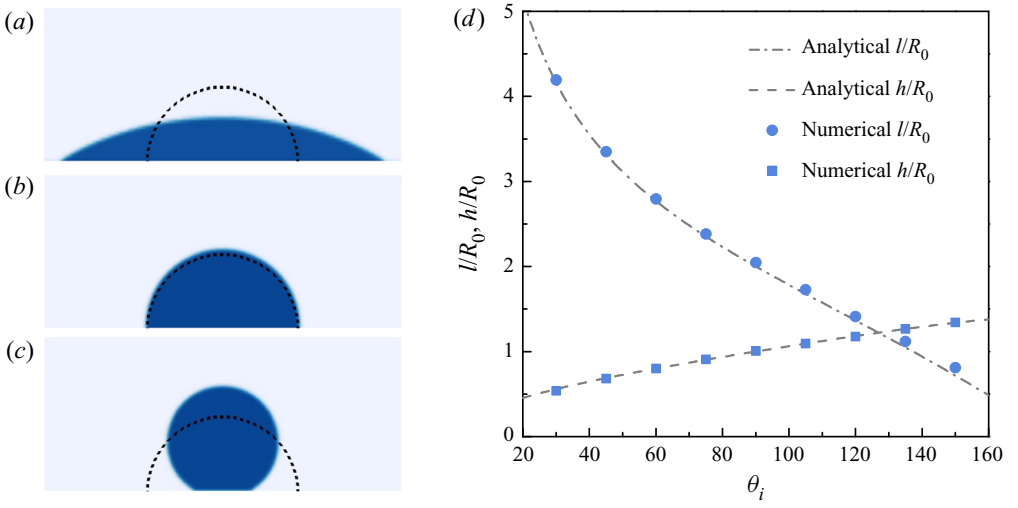

Figure 19. Droplet wetting/dewetting on a flat (*a*) hydrophilic, (*b*) neutral wetting and (*c*) hydrophobic surface, where the black dashed lines and contours represent the initial and equilibrium shapes of the droplet, respectively. (*d*) Analytical and numerical results of spreading length and droplet height for different inherent contact angles θ_i.

with different wettability and measure the spreading length l and droplet height h. It is noted that the interface is located where $\rho_1 = \rho_2$. By the law of mass conservation, the analytical values of l and h are derived as

$$l = 2R_0 \sin\theta_i \sqrt{\frac{\pi}{2(\theta_i - \sin\theta_i \cos\theta_i)}}, \tag{B1a}$$

$$h = R_0(1 - \cos\theta_i) \sqrt{\frac{\pi}{2(\theta_i - \sin\theta_i \cos\theta_i)}}. \tag{B1b}$$

Figure 19(*d*) shows that our numerical results agree well with the analytical solutions.

To further validate the numerical method, droplet evaporation and condensation processes in a homogeneous microchannel driven by a density gradient are simulated. In our set-up, a droplet with a base radius R_0 is initially placed in the middle of a 2-D microchannel with width $b = R_0$. Here R_0 is the characteristic length. The characteristic time T is the total phase transition time of the droplet. The computational domain size is $[0, 12.5] \times [0, 1]$ and the mesh size is 501×41. The inherent contact angle of solid surfaces is supposed to be 75°. The initial equilibrium density distribution of the two components is shown in figures 20(*a*) and 20(*b*), respectively, and the specific initial density profiles are shown in figure 20(*c*).

The boundary conditions are described in Appendix A.3. The Reynolds number Re, the capillary number Ca, the Péclet number Pe and the Cahn number Cn are taken as 0.004, 0.000025, 0.006 and 0.077, respectively. The parameters show that the simulated processes are dominated by diffusion.

Figure 21(*a*,*b*) shows schematic diagrams of the evolution of GLI during droplet evaporation and condensation. The evolutions of V during evaporation and condensation are shown in figure 21(*c*), along with the theoretical predictions given by (A9). We find that our numerical results are consistent with the analytical solutions with small discrepancies at the later stage. The discrepancies may be due to the change of Laplace pressure induced

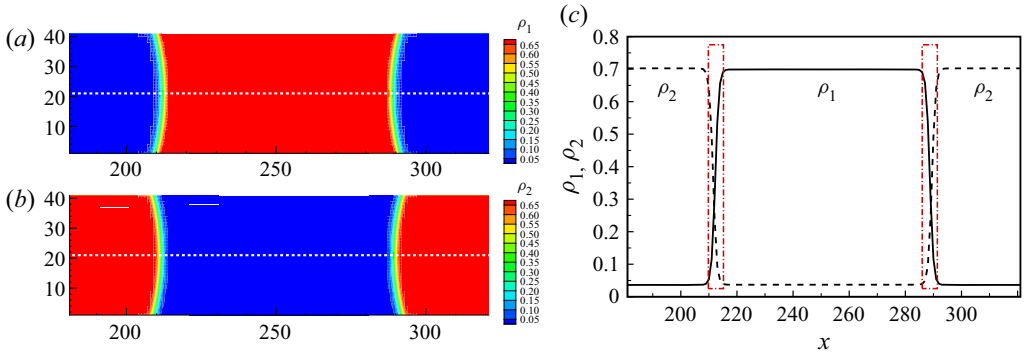

Figure 20. (*a*) Distribution of the density of component 1, i.e. ρ_1. (*b*) Distribution of the density of component 2, i.e. ρ_2. (*c*) Density profiles of components 1 and 2 along the dashed white lines in (*a*,*b*).

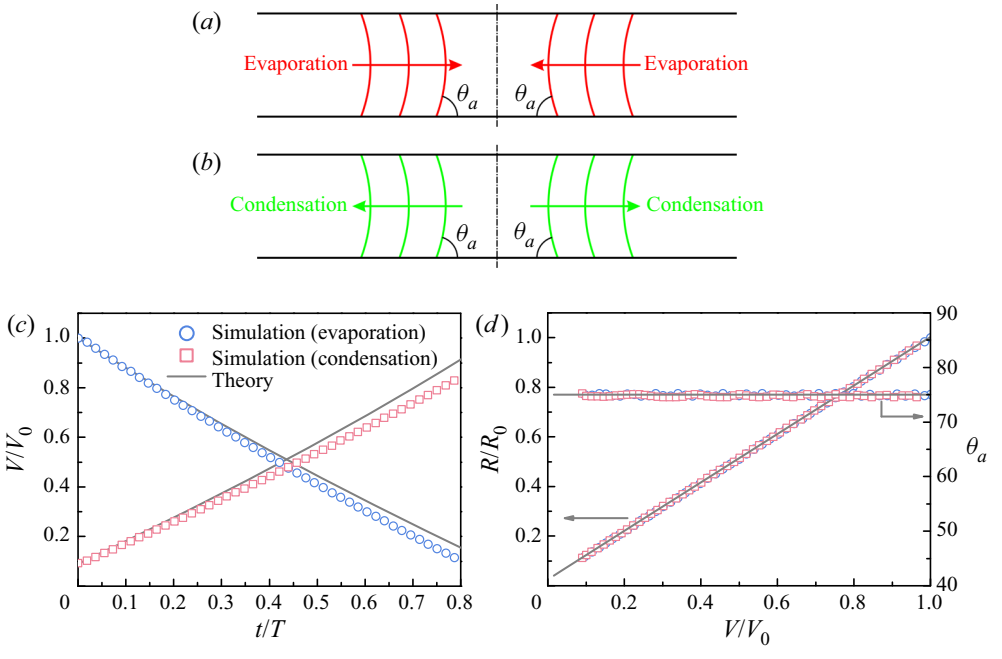

Figure 21. Schematic diagrams of the evolution of GLI during droplet (*a*) evaporation and (*b*) condensation in a chemically homogeneous microchannel. Red and green solid lines represent the GLI during evaporation and condensation, respectively. (*c*) Evolutions of droplet volume V during evaporation and condensation. (*d*) Droplet base radius R and apparent contact angle θ_a as functions of V during evaporation and condensation.

by droplet evaporation/condensation (Hessling *et al.* 2017). In addition, the evolutions of droplet base radius R and apparent contact angle θ_a are shown in figure 21(*d*). It can be seen that θ_a is equal to the supposed inherent contact angle, and the change of R is consistent with the prediction of (2.1). In general, our numerical method is well validated.

References

Bonn, D., Eggers, J., Indekeu, J., Meunier, J. & Rolley, E. 2009 Wetting and spreading. *Rev. Mod. Phys.* **81** (2), 739–805.

BRANDON, S., HAIMOVICH, N., YEGER, E. & MARMUR, A. 2003 Partial wetting of chemically patterned surfaces: the effect of drop size. *J. Colloid Interface Sci.* **263** (1), 237–243.

BRANDON, S. & MARMUR, A. 1996 Simulation of contact angle hysteresis on chemically heterogeneous surfaces. *J. Colloid Interface Sci.* **183** (2), 351–355.

CASSIE, A.B.D. & BAXTER, S. 1944 Wettability of porous surfaces. *Trans. Faraday Soc.* **40**, 546–551.

CHAI, Z.-H. & ZHAO, T.-S. 2012 A pseudopotential-based multiple-relaxation-time lattice Boltzmann model for multicomponent/multiphase flows. *Acta Mechanica Sin.* **28** (4), 983–992.

CHANG, X., HUANG, H., CHENG, Y.-P. & LU, X.-Y. 2019 Lattice Boltzmann study of pool boiling heat transfer enhancement on structured surfaces. *Intl J. Heat Mass Transfer* **139**, 588–599.

CHANG, X., HUANG, H. & LU, X.-Y. 2017 Thermal lattice Boltzmann study of three-dimensional bubble growth in quiescent liquid. *Comput. Fluids* **159**, 232–242.

CRASSOUS, J. & CHARLAIX, E. 1994 Contact angle hysteresis on a heterogeneous surface: solution in the limit of a weakly distorted contact line. *Europhys. Lett.* **28** (6), 415–420.

DAVID, R. & NEUMANN, A.W. 2010 Computation of contact lines on randomly heterogeneous surfaces. *Langmuir* **26** (16), 13256–13262.

DE GENNES, P.G. 1985 Wetting: statics and dynamics. *Rev. Mod. Phys.* **57** (3), 827–863.

DELMAS, M., MONTHIOUX, M. & ONDARÇUHU, T. 2011 Contact angle hysteresis at the nanometer scale. *Phys. Rev. Lett.* **106** (13), 136102.

DI MEGLIO, J.-M. 1992 Contact angle hysteresis and interacting surface defects. *Europhys. Lett.* **17** (7), 607–612.

DI MEGLIO, J.-M. & QUÉRÉ, D. 1990 Contact angle hysteresis: a first analysis of the noise of the creeping motion of the contact line. *Europhys. Lett.* **11** (2), 163–168.

EXTRAND, C.W. 2003 Contact angles and hysteresis on surfaces with chemically heterogeneous islands. *Langmuir* **19** (9), 3793–3796.

FAKHARI, A. & BOLSTER, D. 2017 Diffuse interface modeling of three-phase contact line dynamics on curved boundaries: a lattice Boltzmann model for large density and viscosity ratios. *J. Comput. Phys.* **334**, 620–638.

FUENTES, C.A., HATIPOGULLARI, M., VAN HOOF, S., VITRY, Y., DEHAECK, S., DU BOIS, V., LAMBERT, P., COLINET, P., SEVENO, D. & VAN VUURE, A.W. 2019 Contact line stick-slip motion and meniscus evolution on micrometer-size wavy fibres. *J. Colloid Interface Sci.* **540**, 544–553.

GAO, L. & MCCARTHY, T.J. 2006 Contact angle hysteresis explained. *Langmuir* **22** (14), 6234–6237.

GAO, L. & MCCARTHY, T.J. 2007 How wenzel and cassie were wrong. *Langmuir* **23** (7), 3762–3765.

GAO, L. & MCCARTHY, T.J. 2009 An attempt to correct the faulty intuition perpetuated by the Wenzel and Cassie "laws". *Langmuir* **25** (13), 7249–7255.

GIACOMELLO, A., SCHIMMELE, L. & DIETRICH, S. 2016 Wetting hysteresis induced by nanodefects. *Proc. Natl Acad. Sci.* **113** (3), E262–E271.

GROVES, D. & SAVVA, N. 2021 Droplet motion on chemically heterogeneous substrates with mass transfer. I. Two-dimensional dynamics. *Phys. Rev. Fluids* **6** (12), 123601.

GUAN, D., CHARLAIX, E. & TONG, P. 2020 State and rate dependent contact line dynamics over an aging soft surface. *Phys. Rev. Lett.* **124** (18), 188003.

GUAN, D., WANG, Y.J., CHARLAIX, E. & TONG, P. 2016 Asymmetric and speed-dependent capillary force hysteresis and relaxation of a suddenly stopped moving contact line. *Phys. Rev. Lett.* **116** (6), 066102.

HATIPOGULLARI, M., WYLOCK, C., PRADAS, M., KALLIADASIS, S. & COLINET, P. 2019 Contact angle hysteresis in a microchannel: statics. *Phys. Rev. Fluids* **4** (4), 044008.

HESSLING, D., XIE, Q. & HARTING, J. 2017 Diffusion dominated evaporation in multicomponent lattice Boltzmann simulations. *J. Chem. Phys.* **146** (5), 054111.

HUANG, H., SUKOP, M.C. & LU, X.-Y. 2015 Multiphase lattice Boltzmann methods: theory and application. Wiley–Blackwell.

IWAMATSU, M. 2006 Contact angle hysteresis of cylindrical drops on chemically heterogeneous striped surfaces. *J. Colloid Interface Sci.* **297** (2), 772–777.

JOANNY, J.F. & DE GENNES, P.G. 1984 A model for contact angle hysteresis. *J. Chem. Phys.* **81** (1), 552–562.

KUSUMAATMAJA, H., HEMINGWAY, E.J. & FIELDING, S.M. 2016 Moving contact line dynamics: from diffuse to sharp interfaces. *J. Fluid Mech.* **788**, 209–227.

KUSUMAATMAJA, H. & YEOMANS, J.M. 2007 Modeling contact angle hysteresis on chemically patterned and superhydrophobic surfaces. *Langmuir* **23** (11), 6019–6032.

LEDESMA-AGUILAR, R., VELLA, D. & YEOMANS, J.M. 2014 Lattice-Boltzmann simulations of droplet evaporation. *Soft Matter* **10** (41), 8267–8275.

LHERMEROUT, R. & DAVITT, K. 2018 Controlled defects to link wetting properties to surface heterogeneity. *Soft Matter* **14** (42), 8643–8650.

MARMUR, A. 1994*a* Contact angle hysteresis on heterogeneous smooth surfaces. *J. Colloid Interface Sci.* **168** (1), 40–46.

MARMUR, A. 1994*b* Thermodynamic aspects of contact angle hysteresis. *Adv. Colloid Interface Sci.* **50**, 121–141.

MARMUR, A. 2009 Solid-surface characterization by wetting. *Annu. Rev. Mater. Res.* **39**, 473–489.

MARMUR, A. & BITTOUN, E. 2009 When Wenzel and Cassie are right: reconciling local and global considerations. *Langmuir* **25** (3), 1277–1281.

MCHALE, G. 2007 Cassie and Wenzel: were they really so wrong? *Langmuir* **23** (15), 8200–8205.

MEIRON, T.S., MARMUR, A. & SAGUY, I.S. 2004 Contact angle measurement on rough surfaces. *J. Colloid Interface Sci.* **274** (2), 637–644.

MONTES RUIZ-CABELLO, F.J., RODRÍGUEZ-VALVERDE, M.A., MARMUR, A. & CABRERIZO-VÍLCHEZ, M.A. 2011 Comparison of sessile drop and captive bubble methods on rough homogeneous surfaces: a numerical study. *Langmuir* **27** (15), 9638–9643.

NADKARNI, G.D. & GAROFF, S. 1992 An investigation of microscopic aspects of contact angle hysteresis: pinning of the contact line on a single defect. *Europhys. Lett.* **20** (6), 523–528.

OREJON, D., SEFIANE, K. & SHANAHAN, M.E.R. 2011 Stick-slip of evaporating droplets: substrate hydrophobicity and nanoparticle concentration. *Langmuir* **27** (21), 12834–12843.

OZCELIK, H.G., SATIROGLU, E. & BARISIK, M. 2020 Size dependent influence of contact line pinning on wetting of nano-textured/patterned silica surfaces. *Nanoscale* **12** (41), 21376–21391.

PANCHAGNULA, M.V. & VEDANTAM, S. 2007 Comment on how Wenzel and Cassie were wrong by Gao and McCarthy. *Langmuir* **23** (26), 13242–13242.

PERRIN, H., LHERMEROUT, R., DAVITT, K., ROLLEY, E. & ANDREOTTI, B. 2016 Defects at the nanoscale impact contact line motion at all scales. *Phys. Rev. Lett.* **116** (18), 184502.

POPOV, Y.O. 2005 Evaporative deposition patterns: spatial dimensions of the deposit. *Phys. Rev.* E **71** (3), 036313.

PRADAS, M., SAVVA, N., BENZIGER, J.B., KEVREKIDIS, I.G. & KALLIADASIS, S. 2016 Dynamics of fattening and thinning 2d sessile droplets. *Langmuir* **32** (19), 4736–4745.

PRIEST, C., SEDEV, R. & RALSTON, J. 2007 Asymmetric wetting hysteresis on chemical defects. *Phys. Rev. Lett.* **99** (2), 026103.

PRIEST, C., SEDEV, R. & RALSTON, J. 2013 A quantitative experimental study of wetting hysteresis on discrete and continuous chemical heterogeneities. *Colloid Polym. Sci.* **291** (2), 271–277.

QUÉRÉ, D. 2008 Wetting and roughness. *Annu. Rev. Mater. Res.* **38**, 71–99.

RAMOS, S.M.M., CHARLAIX, E., BENYAGOUB, A. & TOULEMONDE, M. 2003 Wetting on nanorough surfaces. *Phys. Rev.* E **67** (3), 031604.

REYSSAT, M. & QUÉRÉ, D. 2009 Contact angle hysteresis generated by strong dilute defects. *J. Phys. Chem.* B **113** (12), 3906–3909.

SAVVA, N., GROVES, D. & KALLIADASIS, S. 2019 Droplet dynamics on chemically heterogeneous substrates. *J. Fluid Mech.* **859**, 321–361.

SAVVA, N. & KALLIADASIS, S. 2013 Droplet motion on inclined heterogeneous substrates. *J. Fluid Mech.* **725**, 462–491.

SAVVA, N., KALLIADASIS, S. & PAVLIOTIS, G.A. 2010 Two-dimensional droplet spreading over random topographical substrates. *Phys. Rev. Lett.* **104** (8), 084501.

SHAN, X. & CHEN, H. 1993 Lattice Boltzmann model for simulating flows with multiple phases and components. *Phys. Rev.* E **47** (3), 1815–1819.

SHAN, X. & DOOLEN, G. 1995 Multicomponent Lattice-Boltzmann model with interparticle interaction. *J. Stat. Phys.* **81** (1), 379–393.

WANG, X.-P., QIAN, T. & SHENG, P. 2008 Moving contact line on chemically patterned surfaces. *J. Fluid Mech.* **605**, 59–78.

WANG, Y.J., GUO, S., CHEN, H.-Y. & TONG, P. 2016 Understanding contact angle hysteresis on an ambient solid surface. *Phys. Rev.* E **93** (5), 052802.

WENZEL, R.N. 1936 Resistance of solid surfaces to wetting by water. *Ind. Engng Chem.* **28** (8), 988–994.

WU, Y., WANG, F., SELZER, M. & NESTLER, B. 2019 Droplets on chemically patterned surface: a local free-energy minima analysis. *Phys. Rev.* E **100** (4), 041102.

XIE, Q. & HARTING, J. 2019 The effect of the liquid layer thickness on the dissolution of immersed surface droplets. *Soft Matter* **15** (32), 6461–6468.

XU, X. & WANG, X. 2011 Analysis of wetting and contact angle hysteresis on chemically patterned surfaces. *SIAM J. Appl. Math.* **71** (5), 1753–1779.

ZHANG, J., HUANG, H. & LU, X.-Y. 2019 Pinning-depinning mechanism of the contact line during evaporation of nanodroplets on heated heterogeneous surfaces: a molecular dynamics simulation. *Langmuir* **35** (19), 6356–6366.

ZHANG, J., MÜLLER-PLATHE, F. & LEROY, F. 2015 Pinning of the contact line during evaporation on heterogeneous surfaces: slowdown or temporary immobilization? Insights from a nanoscale study. *Langmuir* **31** (27), 7544–7552.

ZIEGLER, D.P. 1993 Boundary conditions for lattice Boltzmann simulations. *J. Stat. Phys.* **71** (5), 1171–1177.